The magmatic–hydrothermal transition in rare-element pegmatites from southeast Ireland: LA-ICP-MS chemical mapping of muscovite and columbite–tantalite

David Kaeter[a,b,*], Renata Barros[b], Julian F. Menuge[a,b], David M. Chew[a,c]
[a]*Irish Centre for Research in Applied Geosciences (iCRAG),University College Dublin, Dublin 4, Ireland*
[b]*School of Earth Sciences, University College Dublin, Dublin 4, Ireland*
[c]*Department of Geology, School of Natural Sciences, Trinity College Dublin, Dublin 2, Ireland*

*Corresponding author. E-mail address: david.kaeter@icrag-centre.org

Abstract

The processes involved in the magmatic–hydrothermal transition in rare-element pegmatite crystallization are obscure, and the role of hydrothermal mechanisms in producing economic concentrations of rare elements such as tantalum remains contentious. To decipher the paragenetic information encoded in zoned minerals crystallized during the magmatic–hydrothermal transition, we applied SEM-EDS and LA-ICP-MS chemical mapping to muscovite- and columbite-group minerals (CGM) from a rare-element pegmatite of the albite-spodumene subtype from Aclare, southeast Ireland.

We present a three-stage model for the magmatic–hydrothermal transition based on petrography, imaging and quantification of rare-element (Li, B, Rb, Nb, Sn, Cs, Ba, Ta, W, U) zoning, integrated with geochemical modeling and constraints from published literature. Stage I marks the end of purely magmatic crystallization from a peraluminous granitic melt. In stage II, polymerized silicic melt and depolymerized alkaline aqueous melt coexist as immiscible media, both of which influence muscovite and CGM crystallization. Stage II also marks the onset of phyllic alteration of primary mineral assemblages. Hydrothermal fluid release causes further resorption of primary minerals and eventual precipitation of fine-grained albite in stage III.

Muscovite and CGM both exhibit trace-element zoning, while CGM also show major-element zoning. Petrographic relationships and geochemical markers such as Ta# (=Ta/[Ta+Nb]) of individual mineral zones reveal that both mineral species crystallized contemporaneously over all three stages. Furthermore, Rayleigh fractional crystallization of muscovite is efficient in fractionating Ta from Nb. Tantalum and Nb are additionally fractionated by halogen-rich aqueous media, which remobilize both elements, but redeposit

preferentially Ta-enriched oxides. Columbite–tantalite mineralization is therefore both magmatic and hydrothermal. Albite associated with stage-III muscovite and CGM was likely precipitated from a hydrothermal fluid when pH changed due to hydrolysis of primary minerals. The complex zoning and resorption of minerals indicates that bulk analyses and conventional LA-ICP-MS spot ablation analyses of muscovite in rare element pegmatites may lead to erroneous modelling of element partitioning and fluid evolution.

Combined petrographic and high-resolution geochemical analysis of two mineral species (which co-crystallize and incorporate the same elements of interest) is an effective tool to assess the complex processes of crystal–melt–fluid interaction. Our three-stage model may also be applicable to the still not well understood magmatic–hydrothermal transition from fertile granitic melts to formation of Sn-W veins and greisens or porphyry-type deposits.

1. Introduction

Understanding mineralization processes is essential for the exploration and optimal exploitation of rare-element pegmatites for metals such as lithium (Li) or tantalum (Ta) (Černý and Ercit 1989). While Li can be extracted from other sources like brine deposits, Ta is mainly sourced from rare-element granites and pegmatites or from placer deposits derived therefrom. Even though the growth in Ta demand has waned since 2000 (Nassar, 2017), Ta remains an important strategic raw material widely used in automobile parts, consumer electronics and high-performance alloys (Linnen et al., 2014). However, controls on Ta in pegmatites and the fractionation of Ta from niobium (Nb) as well as the influence of hydrothermal processes are still not well understood (Van Lichtervelde et al., 2008). Based on experimental work (Linnen, 1998) and observations from Li-Cs-Ta-enriched (LCT) pegmatites at Brazil Lake in Nova Scotia, Canada, Kontak (2006) proposed that the main phase of Nb–Ta mineralization crystallized from a sodium-enriched residual melt after crystallization of primary minerals. Tantalum mineralization associated with albitization of alkali feldspar is common in LCT pegmatites and the abundant occurrence of such replacement bodies is used as an indicator for economic Ta potential (Möller and Morteani, 1987).

Secondary Ta oxides potentially associated with late hydrothermal alteration and formation of quartz and muscovite can be found in several LCT pegmatites worldwide (e.g. Foord and Cook, 1989; Partington et al., 1995; Lumpkin, 1998; Sweetapple and Collins, 2002; Van Lichtervelde et al., 2008; Anderson et al., 2013). Many of these studies are based

on petrographic observations, but the common textural complexity of pegmatites impedes a clear differentiation of primary from secondary textures (Van Lichtervelde et al., 2008). Nevertheless, the consensus is that the main Ta mineralization stage appears late in the pegmatite-forming process. Most researchers agree that fluid exsolution occurs during pegmatite formation, which is documented by miarolitic cavities, fluid inclusions, as well as stable isotope (H, B, O) fractionation (Thomas et al., 2012; Thomas and Davidson, 2013; London, 2014; Siegel et al., 2016; Thomas and Davidson, 2016). However, the timing of fluid release is still debated. Furthermore, the significance of melt–melt immiscibility and fluid exsolution for rare-element mineralization in pegmatites remains contentious (Thomas et al., 2012; Siegel et al., 2016)

Characterizing the chemical variation in zoned minerals using modern *in-situ* micro-analytical methods can yield important constraints on changes in crystallization conditions in magmatic, metasomatic and hydrothermal systems (Ginibre et al., 2007). Micas are ideal for this type of approach. They are the third most common mineral group in granitic pegmatites (Hawthorne and Černý, 1982), are stable over a wide range of physicochemical environments (Tischendorf et al., 1997), and incorporate many rare elements such as Li, Be, B, Rb, Cs, Ba, Sn, Nb and Ta (Fleet et al., 2003), which are indicators of geochemical evolution. Furthermore, muscovite may maintain chemical equilibrium with melt due to fast recrystallization under conditions close to the liquidus (London, 2005). Therefore, mica geochemistry in lithium pegmatites has been studied widely (e.g. Jolliff et al., 1987; Roda-Robles et al., 1995; Wise, 1995; Pesquera et al., 1999; Neiva, 2013; Marchal et al., 2014).

Geochemical analysis of mica is also an important exploration tool for Ta-rich pegmatites (Selway et al., 2005) as empirical data show that mean concentrations of >65–70 ppm Ta and >500 ppm Cs in muscovite indicate high potential for economic Ta mineralization (Gordiyenko, 1971; Morteani and Gaupp, 1989; Selway et al., 2005). A decreasing K/Rb ratio over a suite of muscovite samples is a marker for increasing fractionation and typically coupled with increasing concentrations of incompatible elements (Černý and Burt, 1984). However, although trace elements in micas are routinely analyzed in rare-element pegmatite exploration studies, published data for Sn and high-field-strength elements (HFSE: Zr, Nb, Hf, Ta, W, U) are rare, and most studies employ bulk analyses of mica separates. Such analyses cannot detect internal zoning, multiple generations of mica growth or mineral inclusions within mica crystals, and hence high-resolution *in-situ* micro-analytical methods are preferable (see also Van Lichtervelde et al., 2008; Roda-Robles et al., 2012).

Columbite group minerals (CGM, columbite–tantalite, $[Mn,Fe][Ta,Nb]_2O_6$), which are the main economic host for Ta in rare-element pegmatites (Linnen et al., 2012), are also potentially useful targets for studying melt evolution. These oxides are usually strongly zoned, exhibiting a wide range of chemical compositions. They typically show signs of partial digestion and later overgrowths, and appear to grow during all stages of pegmatite formation (Černý and Ercit, 1985; Lahti, 1987; Mulja et al., 1996; Tindle and Breaks, 2000). Oscillatory zoning and irregular or patchy zoning are common, and magmatic CGM usually show zoning trends with increasing Mn# (=Mn/[Mn+Fe]) and Ta# (=Ta/[Ta+Nb]) from core to rim, referred to as normal zoning (Lahti, 1987). Increasing Mn# and Ta# is typically coupled with increasing fractionation of the pegmatite-forming melt (Linnen and Cuney, 2005; and references therein). While it is commonly assumed that Ta# is directly coupled to fractional crystallization of CGM, Stepanov et al. (2014) demonstrated that Ta# can be controlled by partial melting and fractional crystallization of mica. Mn# is additionally controlled by the crystallization of Mn-/Fe-bearing minerals (e.g. Linnen and Cuney, 2005; Van Lichtervelde et al., 2006; Neiva, 2013). Besides major element zoning, trace element zoning is also likely, but again *in-situ* trace element analyses of CGM are rare.

In-situ analysis of major and minor elements is routinely achieved with high spatial resolution (<5 µm) using scanning electron microscopy (SEM) or electron probe microanalysis. Laser ablation inductively-coupled plasma mass spectrometry (LA-ICP-MS) can achieve significantly better detection limits and is hence preferable for many *in-situ* trace element analyses (Ubide et al., 2015; Sylvester and Jackson, 2016). Conventional LA-ICP-MS spot ablation analyses employ laser pit diameters of 30–50 µm and tens of micrometers depth, often larger than CGM growth zones. This can be circumvented by recent advances in high-resolution spatial LA-ICP-MS chemical mapping (e.g. Ubide et al., 2015).

In this study, we applied the quantitative LA-ICP-MS chemical mapping approach to white mica and CGM from a rare-element pegmatite from Aclare, southeast Ireland. We compare intra- as well as inter-grain element patterns and test whether trace element variations in muscovite, which crystallizes during the entire magmatic–hydrothermal transition, can be explained by Rayleigh fractional crystallization. These data are integrated with petrographic information and correlation of white mica and CGM geochemistry to produce a crystallization model for the magmatic–hydrothermal transition in the studied drill core.

2. Geologic setting, previous studies, and sample material

The Leinster pegmatite belt is located at the eastern margin of the Caledonian S-type Leinster Batholith in southeast Ireland. The LCT pegmatite dikes are of the albite-spodumene sub-type (Černý and Ercit, 2005) and were intruded along the contact zone between the Leinster Batholith and Ordovician metasedimentary rocks (Fig. 1). The dikes strike NE-SW and were emplaced along the regional East Carlow Deformation Zone (ECDZ). The ECDZ is characterized by dip-slip ductile shear expressed by strong foliation of both granite and schist, parallel to the earlier S_1 regional cleavage (McArdle and Kennedy, 1985). No evidence has been found for significant metamorphic or tectonic overprinting of the Leinster rare-element pegmatites (McArdle and Kennan, 1988), which simplifies interpretation of the pegmatite-forming processes.

The Leinster pegmatite belt has been the target of exploration drilling and academic research since the 1970s (e.g. Steiger and von Knorring, 1974; Luecke, 1981; O'Connor et al., 1991). Barros and Menuge (2016) provide a lithological description of the pegmatites and their host rocks at Aclare and Moylisha. However, rare-element and specifically Nb–Ta mineralization has received little attention in earlier studies.

Earlier studies have proposed that the pegmatites crystallized from highly fractionated residual melts of Li-enriched granitic magma (O'Connor et al., 1991). However recent geochemical modelling has shown that this mechanism is unlikely and the pegmatite melt probably formed from anatexis of metasediments (Barros and Menuge, 2016). An anatectic origin by partial melting of metasediments in the ECDZ was also postulated by McArdle and Kennan (1992).

The samples in this study are from a ~10-m-long drill core interval from Aclare (provided by Blackstairs Lithium Ltd, core ACL13-05, ~60 m in total), where several albite-spodumene pegmatite dikes up to ~20 meters thick intrude foliated granodiorite and andalusite-bearing quartz-mica schist. The albite-spodumene pegmatites at Aclare were examined in hundreds of meter of drill core, in boulders and in over 100 thin sections made from this material. Blackstairs Lithium Ltd provided lithogeochemistry data. Samples for this study were selected based on textural features such as replacement or overprint of early pegmatitic units as well as high concentrations of rare-elements such as Be, Rb, Mn, Sn, Cs, and Ta, characteristic of the most evolved parts of the pegmatite. Albitite associated with CGM and cassiterite is abundant, and albitization of microcline as well as muscovitization of spodumene are evident. Following petrographic and mineralogical characterization (optical

microscopy, SEM coupled with energy-dispersive X-ray spectroscopy [EDS]) of 100 µm-thick polished thin sections, two representative thin sections of the albitized parts and one thin section of a coarse-grained quartz–muscovite assemblage were selected for LA-ICP-MS chemical mapping.

3. Analytical methods

3.1. SEM-EDS

Back-scattered electron (BSE) imaging and quantitative major-element analyses of white mica, albite, alkali feldspar, and CGM were carried out at the iCRAG laboratory at Trinity College Dublin (TCD).

Silicates were analyzed using a Tescan TIGER Mira III field-emission (FE) SEM equipped with two Oxford X-Max^N 150 mm^2 EDS detectors. The instrument was calibrated using natural minerals (albite [Na, Al, Si], apatite [Ca, P, F], almandine [Fe, Mg], orthoclase [K], pollucite [Cs]) and synthetic rubidium titanium phosphate (Rb). The reference materials were prepared by Astimex Standards Ltd, Toronto, Canada.

Columbite group minerals were analyzed using a Tescan Mira II FE SEM. The microscope is equipped with an Oxford X-Max^N 150 mm^2 EDS detector. The instrument was calibrated using pyrite (for Fe) and pure metals (Mn, Ta, Nb). The reference materials were prepared by Micro-Analysis Consultants Ltd, Cambridgeshire, United Kingdom.

With both instruments, quantitative analyses were performed at 20 kV acceleration voltage and ~0.3 nA beam current. Energy-dispersive X-ray spectra with at least 3,000,000 total counts per spectrum were acquired using the Oxford Aztec software with a process time setting of 5. The working distances (WD) were 15 mm (TIGER) and 18 mm (Mira II). Before each measurement, samples were focused using the z-control of the SEM stage without changing the WD. Detection limits were below 0.1 wt% for most elements. Beam calibration was performed on cobalt metal. Polished samples, reference materials, and cobalt metal were carbon coated (~13 nm) before analysis.

Reproducibility of major element silicate analyses using the TIGER SEM was monitored over 6 months using stoichiometric diopside (n = 8) and orthoclase (n = 6) as quality control materials. The standard deviation (1σ) for SiO_2 in both minerals over this time period is below 1%. The data quality of quantitative SEM-EDS data presented in this study is assessed in more detail in Supplementary Note A.2.

206

207 *3.2. LA-ICP-MS chemical mapping*

208 Trace element mapping was carried out with a Photon Machines Analyte Excite
209 193 nm ArF Excimer laser-ablation system with a Helex 2-volume ablation cell coupled to an
210 Agilent 7900 quadrupole ICP-MS at the iCRAG laboratory at TCD.

211 White mica and alkali feldspar were mapped using a suite of fifteen isotopes (^{7}Li, ^{11}B,
212 ^{23}Na, ^{27}Al, ^{28}Si, ^{39}K, ^{47}Ti, ^{55}Mn, ^{71}Ga, ^{85}Rb, ^{93}Nb, ^{118}Sn, ^{133}Cs, ^{137}Ba, ^{181}Ta). A modified set
213 of isotopes (^{7}Li, ^{11}B, ^{28}Si, ^{39}K, ^{45}Sc, ^{47}Ti, ^{85}Rb, ^{89}Y, ^{93}Nb, ^{118}Sn, ^{133}Cs, ^{137}Ba, ^{181}Ta, ^{182}W,
214 ^{238}U) was acquired while mapping CGM, which was also used for one white mica
215 experiment. The laser repetition rate was 55 Hz and the fluence was 3.9 J/cm^2 for all
216 experiments. The mass spectrometer was tuned using line scans on NIST612 glass reference
217 material (Jochum et al., 2011) to yield stable Th/U ratios of unity and low oxide production
218 rates at the beginning of each analytical session.

219 Element image maps were created by successively acquiring adjacent lines to produce
220 a rectangular mapped area. A square-shaped laser aperture was used with a laser spot
221 diameter (d_s) of 7, 10, or 18 µm depending on the size of the mineral area of interest. The
222 scan speed was either 10 µm/s (d_s = 7, 10 µm) or 30 µm/s (d_s = 18 µm). Each individual
223 experiment commenced and finished with two line scans on NIST610 glass (Jochum et al.,
224 2011), which was used as the primary reference material. The ablation depth is very shallow
225 (< 1 µm) as indicated in supplementary Fig. A.1 (Supplementary Note A.1), which is
226 assessed in greater detail in Ubide et al. (2015).

227 The Iolite v3 software (Paton et al., 2011) was used for data reduction and production
228 of trace element images. The data was processed using a modified version of Iolite's
229 "Trace_Elements" data reduction scheme (DRS) (Ubide et al., 2015). Besides data reduction
230 for trace element analyses, this modified DRS additionally allows calculation of elemental
231 ratios and generation of images therefrom. Silicon concentrations of white mica and feldspar
232 as determined by SEM-EDS were used as the internal standard for the calibration of silicate
233 LA-ICP-MS data. Due to strong CGM heterogeneity, CGM data was processed without an
234 internal standard element using the semi-quantitative mode of the same DRS. After data
235 reduction, trace element ratios were calculated, and images were created using the "Image
236 from integrations" feature of Iolite. A comprehensive description of the experimental setup
237 and data reduction can be found in Ubide et al. (2015).

238 The resulting semi-quantitative element concentrations in CGM were extracted by
239 defining regions of interest (ROIs), which can be regarded as 'pseudo-laser spots', in the

elemental image using the Iolite extension Monocle (Petrus et al., 2017) in small, homogenous areas (according to BSE imaging), where the major element chemistry had previously been determined by SEM-EDS. A correction factor was calculated by dividing the Ta concentration calculated with Iolite by the Ta concentration obtained by SEM-EDS (f_c = $[Ta]_{Iolite}/[Ta]_{SEM-EDS}$). This correction factor was then used to calculate the concentrations of the remaining elements ($[X] = [X]_{Iolite}/f_c$). Due to the large difference in Ta concentration between NIST610 (~446 ppm, Jochum et al., 2011) and the CGM in this study (15–40 wt%), as well as micron-scale inhomogeneities in CGM, these concentrations are regarded as semi-quantitative, but relative differences in trace element zoning are unaffected.

The fully quantitative white mica data was extracted by defining ROIs which correspond to distinct crystal zones using Monocle. This data was then utilized to compare the compositions of different growth zones and evaluate fractionation trends within single crystals, as well as between the three samples. Example muscovite ROIs are shown in supplementary Fig. A.2 (Supplementary Note A.1) The boundaries of each zone and the outer portions of the grain rim were avoided to prevent extracting mixed signals from adjacent zones or the matrix. Additional ROIs were defined to extract whole-grain compositions. The whole-grain data is compared to K and minor-element data from SEM-EDS in Supplementary Note A.3. Most deviations between the two data sets can be explained by the low precision of SEM-EDS for minor elements. However, analyses of the major element K are more accurate using SEM-EDS. Therefore, the K LA-ICP-MS data used for element ratios was adjusted by linear regression of the two data sets as described in Supplementary Note A.3. Errors presented for LA-ICP-MS data are 2 standard errors (2SE) for the average concentration of individual ROIs.

4. Mineralogy

The studied drill core interval can be subdivided into three lithologies: a) a coarse pegmatitic mineral assemblage (Fig. 2a) characterized by variable proportions of centimeter-scale quartz (20–50%), muscovite (10–50%), spodumene (0–20%) and perthitic microcline (0–35%); b) a fine-grained (usually < 1 mm) albitite (Fig. 2b) comprising lath-shaped albite (>85– 90%) with quartz and yellow muscovite; and c) assemblages with equal proportions of coarse dark-green muscovite and dark gray quartz (5–20 mm, Fig. 2c) that comprise ~10% of the pegmatite drill core intersection, which are typically interfingered with or pervaded by albitite. Spodumene in (a), muscovite (a, b) and albite (b) are preferentially aligned

subparallel to the pegmatite contact and the granodiorite country-rock foliation. Muscovite shows generally very pronounced cleavage planes; violet fluorite along cleavage planes occurs in some grains. Apart from rare fine-grained epitaxial overgrowths, muscovite appears optically homogenous. Accessories in all lithologies include fine-grained (<2 mm) dark blue anhedral to subhedral Mn-rich F-apatite, colorless beryl, orange spessartine garnet, zircon, and interstitial brown sphalerite.

A distinct lithological zonation with paragenetic changes from border to center often observed in other granitic pegmatites is absent in this drill core intersection. However, spodumene crystallized early assuming crystallization from the outer contact towards the center of the pegmatite, because the main spodumene-bearing interval (~15% over 2.5 m) is located close to the hanging wall.

The term sodic aplite is sometimes used to refer to parts of granitic pegmatites formed by late or secondary albitization (lithology b), but this can lead to confusion with aplites in pegmatite borders. For clarity and consistency, *albitite* will be used in the following to refer to the fine-grained lithology, which is dominated (usually >90%) by platy or lath-shaped albite associated with replacement of primary minerals.

In the pegmatitic lithology (a), quartz exhibits undulose extinction and common recrystallization. Microcline shows diffuse crosshatch twinning, albite its typical lamellar twinning and spodumene simple twinning parallel to the long axis of elongate-prismatic crystals. Tabular and anhedral CGM (<2000 µm) occur associated with muscovite and microcline. In albitite (b), lath-shaped, tabular and irregular CGM (20–2000 µm) as well as other Nb–Ta–Sn oxides, such as microlite and wodginite, can occur disseminated or in high local abundance (0–3% total). Albitite is located near the upper and lower margins and is common throughout the whole drill core interval. Replacement textures are preserved especially close to the borders. These textures include albitization and muscovitization of microcline and pseudomorphic replacement of spodumene by fine-grained green muscovite. However, albitite without remnant minerals is also abundant throughout the drill core intersection.

Foliated granite shows about 2–3 cm of greisenization at pegmatite contacts. Here, granodiorite feldspar and biotite are increasingly replaced by white mica towards the pegmatite body. The alignment of white mica is parallel to the granodiorite foliation. Additionally, dark brown tourmaline is observed in granodiorite close to the pegmatite contacts.

Petrographic features of the three pegmatite samples studied in more detail using LA-ICP-MS are described in the following subsections.

4.1. Upper border albitite (UB-A)

Sample UB-A is located near the upper border and consists only of lithology (b). It comprises coarse-grained tabular (~20%, 1000–2000 mm) and fine-grained lath-shaped albite (~50%, 50–500 µm), tabular muscovite (10–15%, 500–2000 µm), anhedral quartz (10%, 500–2000 µm) and coarse subhedral spessartine-rich garnet (<1%, ~1500 µm). Albite shows micro-porosity at high SEM magnification (Fig. 3a, inset). Subhedral elongate-prismatic CGM (100–400 µm, Fig. 3a) are commonly associated with albite, while irregular CGM (100–300 µm) are coeval with coarse muscovite. Tantalum-enriched rims as expressed by higher BSE intensity (Fig. 3a, arrow) are observed for most CGM associated with albitite. Furthermore, some CGM exhibit replacement or overgrowth by microlite (Fig. 3b) and wodginite. Additional accessories are interstitial Mn-rich F-apatite and irregularly-zoned sphalerite. Minor chalcopyrite, pyrite, uraninite, zircon and calcite occur especially as fillings of cavities and fractures. Overall alignment of the crystals is subparallel to the pegmatite–granodiorite contact. Several fractures crosscut the sample at a high angle to the primary foliation. Associated with these fractures are quartz, sulfides, and secondary fine-grained rose-colored mica overgrowing coarse-grained muscovite. Three muscovite grains, one of which is coeval with CGM (Fig. 3c), were selected for LA-ICP-MS mapping.

4.2. Quartz–muscovite assemblage (QM-A)

Sample QM-A is located in the lower half of the drill core and consists mainly (80%) of lithology (c). It is in contact with albitite at its lower end. Coarse-grained silvery dark-green muscovite (5–20 mm) is embedded in a matrix of irregular translucent grey quartz (~50:50). Opaque elongate inclusions between cleavage planes of muscovite are common. Additional phases are rare anhedral colorless beryl and anhedral to subhedral dark orange spessartine (1–2 mm and <1% each, Fig. 3d–e). Accessories include F-apatite, chalcopyrite, pyrite and sphalerite. Isolated patches of albite laths (0.1–1 mm) occur sporadically on quartz and muscovite grain boundaries. Some mica shows replacement by secondary mica (brighter BSE intensity in Fig. 3d–e, arrows). The albititic part of the sample is similar to the fine-grained portion of UB-A (see above). Muscovite in contact with the albitite (one map) as well as inside the quartz–muscovite assemblage (two maps, one in contact with beryl, Fig. 3d) were selected for LA-ICP-MS mapping.

341

342 *4.3. Lower border albitite (LB-A)*

343 In sample LB-A, which is located close to the footwall contact, coarse perthitic
344 microcline (25%, 3–20 mm) of lithology (a) occurs in a matrix of fine-grained albite laths
345 (50%, 0.1–1.5 mm, Fig. 3f) of lithology (b). Albite shows minute elongate-prismatic apatite
346 inclusions (5–25 µm). Microcline is fractured, with crystallization of a very fine-grained
347 intergrowth of rose-colored mica and quartz (20–40 µm, Fig. 3f, inset) along fractures. This
348 replacement is rarely observed for albite and the fractures often do not advance into adjacent
349 albite.

350 Albite laths are preferentially aligned subparallel to the pegmatite margin. No
351 preferred orientation is observed in albite surrounding microcline. Quartz is absent apart from
352 a patch of massive quartz (approx. 10% of the thin section) showing dynamic recrystallization
353 with grains up to 5 mm, associated with pegmatitic microcline. Coarse muscovite occurs as
354 anhedral crystals (up to 3 mm) between microcline and rarely as smaller anhedral flakes
355 (<1 mm) within the albitite matrix. Some muscovite is overgrown by fine-grained mica
356 (arrows in Fig. 3g). Rare zircon with uraninite-rich cores is associated with albite. Accessory
357 zoned sphalerite occurs interstitially.

358 Columbite–tantalite is common as elongate-prismatic subhedral crystals associated
359 with muscovite and microcline as well as within albitite. Grains associated with albitite
360 appear finer grained (50–150 µm, Fig. 4a) and show oscillatory zoning more distinctly than
361 CGM associated with pegmatitic muscovite and microcline (300–500 µm). Coarse CGM
362 appear more irregular, show patchy zoning and common truncation (Fig. 4c). Irregular zones
363 are also visible in CGM within the albite matrix, often overgrown by a Ta-enriched rim
364 (higher BSE intensity, Fig. 4a, arrow). Zoning seems more complex in CGM in this part of
365 the drill core than in the upper border albitite (UB-A), while microlite and other secondary
366 Nb–Ta–Sn oxides are absent. Two muscovite grains, three CGM, and part of a fractured
367 remnant microcline crystal with secondary mica and quartz were selected for LA-ICP-MS
368 mapping.

369

370 **5. Geochemical data**

371

372 Table 1 summarizes all samples and mineral grains analyzed. Mineral chemistry as
373 determined by SEM-EDS and LA-ICP-MS chemical mapping is presented in the following
374 subsections.

375

376 *5.1. Major element chemistry*

377

378 Individual grains were analyzed in at least three locations and the standard deviation
379 (1σ over *n* measurements) for major element concentrations over these measurements is
380 generally low (e.g. usually <0.5% for SiO_2). The standard deviation for minor elements near
381 the detection limit is high, because of low EDS intensities (low signal-to-noise-ratios) as well
382 as potential inhomogeneity for incompatible elements such as Rb and Cs.

383

384 *5.1.1. White mica*

385 Compositions of white mica from all samples are presented in Table 2. Apart from
386 rare alteration rims, which were avoided during analysis, muscovite in all samples is
387 homogenous within analytical precision regarding its major element composition.

388 Besides fine-grained muscovite filling fractures (LB-A-Ms-3), iron and fluorine
389 contents of primary muscovite are high (~1.4–3.5 wt% FeO; 0.4–1.0 wt% F). Furthermore,
390 muscovite from the quartz–muscovite assemblage (Q-MA) is richer in Fe and F than
391 muscovite associated with albitite (UB-A, LB-A). All samples are enriched in Rb and show
392 Cs near the EDS detection limit of 0.03 wt% Cs_2O. The secondary mica QM-A-Ms-2b shows
393 highest concentrations of Fe and F (8.81 wt% FeO; 4.37 wt% F) and elevated Mn and Cs.

394 Accuracy of the data for F, is a potential problem, because of a partial overlap of the F
395 Kα peak with the Fe Lα peak in the EDS spectrum. Therefore, we did not undertake
396 quantitative analysis and interpretation of the presented F data. For a detailed discussion, we
397 refer to Supplementary Notes A.2 and A.3.

398

399 *5.1.2. Feldspar*

400 Compositions of albite (Ab) and microcline (Kfs) in sample LB-A are shown in
401 Table 3. Cation totals are close to stoichiometric formulae. Albite ($Ab_{\sim 99}$) shows little
402 variation. Microcline shows higher variability ($Or_{91–94}$) with up to 0.4 wt% P_2O_5 and
403 detectable amounts of Cs and Rb, but signal-to-noise ratios were too low for quantification.

404

405 *5.1.3. Columbite group minerals*

406 As mentioned in 3.2, data for CGM were derived from sum spectra over small
407 homogenous areas (according to BSE intensity), which are displayed in Fig. 4a–c (circles).
408 Apart from one measurement (LB-A-CGM-3-3), element oxide sums and cation calculations

presented in Table 4 are close to the stoichiometric formula of XY_2O_6. The slightly elevated cation sum for CGM-3-3 (3.05 apfu) might be caused by the presence of Fe^{3+}. Due to likely inhomogeneity even within small areas of crystals, these data need to be handled with caution. These small-scale variations become evident in Fig. 5, which shows a quantitative line scan over LB-A-CGM-1 with ~0.8 µm point spacing. The oscillatory zoning is clearly defined by Ta# (solid red line), while the pattern for Mn# (dotted blue line) is less distinct. Even within narrow zones that appear homogenous in BSE intensity, Mn# can vary strongly. It is furthermore noticeable that the overall increase of Ta# from core to rim is accompanied by generally decreasing Mn#, which slightly increases again within the rims.

5.2 Minor and trace element maps

Selected LA-ICP-MS chemical images of muscovite and CGM are shown and described here for each sample while additional LA-ICP-MS images and accompanying descriptions can be found in Supplementary Note B. Individual zones were defined based on high gradients in concentrations of Cs and Sn, and Ta/Nb for muscovite, and Ta/Nb and other HFSE (Sn, W, U) for CGM. The Ta/Nb ratio in muscovite is related primarily to variations in Ta, as variations in Nb are less pronounced. The mean elemental concentrations of each zone in every grain are summarized in supplementary tables ST1 (micas) and ST2 (CGM).

5.2.1. Upper border albitite (UB-A)

In muscovite UB-A-Ms-1, four distinct zones can be identified (Fig. 6). Texturally, zone 1 comprises small euhedral triangular flakes, overgrown by zone 2, which shows an irregular contact with subhedral zone 3. The large gradient in Cs concentration between zones 3 and 4, and the truncation of zone 3, suggest a hiatus in crystallization. The Ta/Nb ratio is lowest in zone 1 (30 ppm/150 ppm = 0.20) and highest in zone 3 (90 ppm/109 ppm = 0.83). Cesium and Rb are lowest in zone 4 (376 ppm and 3995 ppm) and highest in zone 2 (1359 ppm and 6788 ppm). Zoning of Na and Li appears independent of the zone boundaries and varies between 3150–3490 ppm and 711–844 ppm, respectively. However, both are depleted towards the margins, which correspond to the outer parts of zone 4. Ba shows an enrichment in the margins from 46–63 ppm (zones 1–3) to 74 ppm (4).

441 *5.2.2. Quartz–muscovite assemblage (QM-A)*

442 Grain QM-A-Ms-2a is coarse-grained green muscovite in contact with beryl showing
443 four zones (Fig. 7). Zone 1 comprises several grains of platy to elongate-prismatic mica,
444 which are overgrown by subhedral zone 2, followed by irregular zones 3 and 4, which do not
445 appear to be in contact with each other. Chemically, zone 1 is enriched in Li (3496 ppm), Rb
446 (6193 ppm), Mn (3476 ppm), Sn (564 ppm), and especially Cs (2963 ppm). The second zone
447 is characterized by decreasing concentrations of these elements but elevated Na (2532 ppm).
448 Zone 3 has low concentrations of Li (2607 ppm), Rb (3545 ppm), Cs (442 ppm), Mn
449 (2682 ppm) and Sn (433 ppm). The Ba concentration slightly increases from 45–52 ppm
450 between zones 1 and 3. Zone 4 is similar to zone 3 in most elements, but shows the lowest Ba
451 concentration (22 ppm). Zone 1 shows the highest Ta/Nb (51 ppm/100 ppm = 0.51) and zone
452 4 the lowest (42 ppm/91 ppm = 0.46). The LA-ICP-MS data also show that the secondary Fe-
453 rich mica QM-A-Ms2b, is enriched in Li (8325 ppm), Mn (5170 ppm) and Ta
454 (Ta/Nb = 54 ppm/99 ppm = 0.55).
455
456 *5.2.3. Lower border albitite (LB-A) – White mica and microcline*

457 Muscovite LB-A-Ms-2 (Fig. 8) is a coarse grain in contact with remnant high-Ba
458 microcline, secondary albite (low in all trace elements) and LB-A-Ms-CGM-3 (high Sc, Ti,
459 Sn, W). It exhibits at least six distinct zones. Texturally, the core zone (zone 1) is anhedral
460 and truncated by the subsequent zones. Zones 2–4 appear subhedral to euhedral, while zone 5
461 shows an anhedral boundary. Zone 6 is a sub-epitaxial overgrowth of very fine-grained
462 muscovite.

463 Geochemically, zone 1 is rich in Cs (1197 ppm) and low in Ti (169 ppm) and B
464 (124 ppm). It shows a high Ta/Nb ratio (69 ppm/141 ppm = 0.49) associated with elongated
465 inclusions parallel to the cleavage. Inclusions of plagioclase and quartz occur at the margin of
466 zone 1, in the upper center of each image. Zones 2–4 are characterized by oscillating
467 concentrations of B, Ti, Sn, Ba, Ta and W. Boron and Ba are high in zones 2 and 4 (143–
468 175 ppm B, 9–16 ppm Ba), while Sn, W and Ta are depleted in these zones and are enriched
469 in zone 3 (909 ppm Sn, 5.8 ppm W, Ta/Nb = 118 ppm/169 ppm = 0.70). Rb and Cs show
470 progressive increase from 6356 ppm and 958 ppm in zone 2 to 6487 ppm and 1073 ppm in
471 zone 4, respectively. Zone 5 is characterized by a drop in B (80 ppm), Rb (3323 ppm) and Cs
472 (391 ppm), while Sc (~1 ppm), Ti (365 ppm), Ba (32 ppm), Ta (90 ppm) and W (4.8 ppm) are
473 all elevated compared to zone 4. The Ba image shows that zone 5 appears in direct contact
474 with microcline. Zone 6 is low in most elements except B (113 ppm). Lithium seems largely

independent of the zoning. However, it is highest in the core (928 ppm) and lowest along fractures as well as in zone 6 (603 ppm). Concentrations of Ta and to a lesser extend W are elevated in close proximity to LB-A-CGM-3, which is clearly visible in the Ta/Nb ratio (Fig. 8), possibly caused by diffusion along the steep concentration gradient between the two minerals. This area and high-Ta inclusions elsewhere were avoided when extracting the data. U and Y (not shown) are low and close to their detection limits. Slight enrichment in both elements is visible along fractures and grain boundaries.

Microcline LB-A-Kfs-1 (Fig. B.6a, Supplementary Note B) has low trace element contents, except for enrichment in Rb (~4200 ppm, K/Rb = 35) and Cs (~430 ppm). Furthermore, the analyzed grain is low in Li (17 ppm), B (12 ppm), Mn (~100 ppm), Ga (19 ppm), Sn (3.5 ppm) and Ba (90 ppm). Ta and Nb are below 1 ppm (Ta/Nb = 1.4). Secondary mica associated with fractures crosscutting microcline (LB-A-Ms-3), is too fine-grained to extract quantitative data. Furthermore, the concentrations are likely to be diluted because of the intimate intergrowth with quartz. Nevertheless, its composition can be described qualitatively based on the LA-ICP-MS images (Fig. B.6b): it is similar to zone 6 of LB-A-Ms-2 with 2000–2500 ppm Na, up to 200 ppm Ti, 50–70 ppm Ga, and 2000–3000 ppm Rb. However, it is poorer in Li (<200 ppm), Mn (<300 ppm), Nb (<10 ppm), Sn (<150 ppm) and Ta (<10 ppm).

5.2.4. Lower border albitite (LB-A) – Columbite–tantalite

The extensive zoning of CGM, visible in the BSE images (Fig. 4), is also observed in the minor- and trace-element maps (Fig. 9). For LB-A-CGM-1 (Fig. 9a), Ta/Nb corresponds well with intensity variations observed in the BSE image. Five zones were identified in CGM-1: zone 1 is high in Y (5 ppm), Ti (3130 ppm), Sn (1515 ppm), W (2175 ppm) and U (4890 ppm). Concentrations of these elements drop progressively towards zone 3, where they are lowest. Zone 4 is enriched again in Sn (1065 ppm) and Ti (1700 ppm). Zone 5 shows an enrichment in K (93 ppm), Sc (~9 ppm), and Y (1.5 ppm) and is enriched in Ti (1760 ppm) and W (575 ppm, up to 800 ppm) in the inner part of the zone. The Ta/Nb ratio increases in steps alternating with local minima from zone 2 to 5 as seen in the SEM-EDS data. Strong enrichment in K (>1400 ppm) at the left grain boundary might be caused by alteration. Lithium, Rb, Cs and Ba (not shown) are positively correlated with K.

LB-A-CGM-3 (Fig. 9b) is in contact with muscovite LB-A-Ms-2 (high K) in the pegmatitic portion of the sample and is surrounded by secondary albite. The sequence of zones observed in the other CGM grains is less distinct in CGM-3. However, four zones were

defined on the basis of changing Ta/Nb ratios and trace element contents. The highest Sn (>1600) and W (>900 ppm) were detected in irregular patches (zone 1) with moderate Ta/Nb (1.23). This zone is also enriched in U (3145 ppm), which is additionally concentrated along fractures, as are alkali metals. Zones 2 and 4 are richest in Ta with Ta/Nb of 2.06 and 2.13, respectively. Zone 3 shows low trace element concentrations and the lowest Ta/Nb ratio (0.98). Sn and W show minor variation between zones 2, 3 and 4 (660–800 ppm Sn, 470–630 ppm W). Given the complex texture of CGM-3 as observed in the BSE image, the order of the zones does not necessarily represent the order of crystallization. Petrographically, zone 4 seems to be associated with zone 5 in the adjacent muscovite.

6. Crystallization history and rare-element evolution

6.1. Stages of pegmatite formation

Three individual paragenetic *stages* (I, II, III) with consistent behavior among all analyzed muscovite grains were defined. The geochemical evidence for the individual stages is presented here and a paragenetic model for stage formation is presented in section 7. Each muscovite grain shows petrographic discontinuity between these stages in the respective LA-ICP-MS images and each stage can comprise multiple *zones* (e.g. I.1, I.2, I.3) in one grain. Furthermore, the zones of all grains can be correlated based on fractionation patterns as indicated by their K/Li, K/Rb and K/Cs ratios (Fig. 10a). Petrographic discontinuity was also observed for individual CGM grains and CGM zones were assigned to the same three stages as micas assuming contemporaneous crystallization, the evidence for which is presented in subsection 6.1.3. In the following subsections, chemical variations within each stage are described in more detail, first for muscovite and then for CGM.

The same numbering for two zones in different grains does not necessarily mean contemporaneous crystallization. While this is likely the case for grains within one thin section, onset of crystallization might vary along the length of the drill core or the pegmatite dike system as a whole. The trace element data for each zone determined from the LA-ICP-MS images and their correlation with paragenetic stages is summarized in supplementary Tables ST1 (muscovite) and ST2 (CGM).

6.1.1. Zoning in white mica

Stage I is characterized by decreasing K/Rb, K/Cs (Fig. 10a) as well as an increase in most other trace elements (e.g. Ti, Mn, Nb, Sn, Ta, Fig. 10b). In stage II, K/Rb varies only slightly, but increases again in stage III. For K/Li, contrasting behavior is observed for the central quartz–muscovite assemblages (Q-MA) compared to the border albitite (UB-A, LB-A). In QM-A, K/Li exhibits a local minimum in zone II.2, while UB-A and LB-A show local maxima. The K/Cs ratio additionally shows a strong local minimum in II.2 for most samples. In stage III, alkali metal ratios strongly increase to values sometimes higher than the corresponding ratios in stage I.

The intra-grain patterns for B, Ba and HFSE (Nb, Ti, Sn and Ta/Nb, Fig. 10b), are more complex than for alkali metal ratios. Stage I is characterized by an initial decrease followed by a strong increase for all of these elements except B and Nb. Boron decreases in stage I, while Nb in the central sample (QM-A) initially increases before it decreases again. This increase in Nb is also observed for the border albitite samples. Stage II is characterized by even stronger variations. Boron shows an overall decrease but oscillates between subsequent zones. Similar behavior, but with the opposite amplitude, is observed for Sn, Ta/Nb and to a lesser degree Ti. Barium seems to correlate with B in LB-A-Ms-2, but shows anti-correlation with B for the other grains. Niobium concentrations are high in stage II, but they typically decrease towards stage III. In stage III, most elements decrease, except B. The replacive BSE-bright mica (indicated by an asterisk in Fig. 10) is enriched in Nb and Ba and depleted in Sn relative to stage III.

Individual error bars for element concentrations and element ratios were omitted in Fig. 10 to ensure readability of the diagrams. However, abrupt concentration changes between two zones as observed in K/Li, K/Rb, K/Cs, B, Ti, Sn and Ta/Nb significantly exceed analytical uncertainty.

To investigate element variations within single zones, a concentration profile (Fig. 11) for muscovite LB-A-Ms-2 (along the path A–B–C as shown in the last panel of Fig. 8) was constructed using the average of three parallel lines of adjacent pixels to reduce scatter. Small-scale variations aside, Cs appears to exhibit power-law behavior within zone I.3 and within stage II. Lithium and Rb (not illustrated), show similar behavior to Cs. The behavior of Ba is different: it shows an overall decrease from zones I.3 to II.3 and increases abruptly in stage III. Boron shows anti-correlation with Ta, while Ti and Sn show good correlations with Ta in most zones. Niobium and Ta show more complex behavior; they are positively correlated in stages I and III, but some zones in stage II show anti-correlation.

575

576 *6.1.2. Zoning in columbite group minerals*

577 Zones in CGM of sample LB-A can easily be correlated using their intra-grain trace-
578 element patterns (Fig. 12). Three stages were defined based on petrography and geochemistry
579 and are consistent with the stages described for white mica. All grains show similar patterns
580 for Ti, Y, Sn and Ta/Nb, and correlate well in their overall W and U distribution. Based on
581 these element patterns, zones in CGM-3 could be correlated. The order of crystallization for
582 the zones in CGM-3, difficult to establish petrographically, is 1–3–2–4 as indicated in the
583 plot for Ta/Nb. In stage II, CGM-1 and CGM-3 show opposing patterns in Sn, W and U.
584 Most elements correlate well with Ta/Nb, but vary in detail. Titanium and Sn seem to
585 correlate with Ta/Nb of CGM-2 and in the older zones of the other grains, while Sn behaves
586 differently in CGM-3 after Zone II.1. Apart from Sc, all trace elements are enriched in stage I
587 of each grain. The grains show reverse zoning (decreasing Ta/Nb) in stage I, then normal
588 zoning from zone II.1 onwards. Stage III is characterized by the highest Ta/Nb as well as an
589 increase in Cs, which decreases in stage I and is very low in stage II.

590 The analytical uncertainties for CGM are large especially for LB-A-CGM-1 due to the
591 small grain size and consequently low number of pixels for each ROI. However, distinct
592 concentration changes between two zones significantly exceed analytical uncertainty.

593

594 *6.1.3. Contemporaneous crystallization of muscovite and CGM*

595 Concentration patterns observed for stages I to III for muscovite and CGM suggest
596 contemporaneous crystallization of these phases. Patterns for Sn and Ti for both minerals
597 correlate (Figs. 10b and 12), and patterns for Cs in CGM are similar to the pattern of K/Cs in
598 muscovite (Figs. 10a and 12), which suggests an anti-correlation for the alkali metals. The
599 pattern for Ta# in muscovite also closely resembles that of CGM. This becomes evident when
600 comparing Ta# profiles across LB-A-Ms-2 and LB-A-CGM-1 (Fig. 13a). The grains are
601 about 2 cm apart in the thin section and separated by fine-grained albite, and show almost
602 identical zoning, and similar absolute values of Ta#. Additionally, zone III.1 of LB-A-CGM-
603 3 is spatially closely associated with III.1 of LB-A-Ms-2 and both show high Ta# (0.68 and
604 0.46, respectively). This petrogenetic association is also evident in the composite BSE image
605 (Fig. 13b). Growth of Ms-2-III.1 was furthermore restricted by the contact with earlier (stage
606 I–II) zones of CGM-3.

607

608 *6.2. Rare-element fractionation*

609

610 *6.2.1. Rayleigh fractional crystallization*

611 Hulsbosch et al. (2014) demonstrated that, if a sequence of compositions of a mineral
612 *i* is the product of Rayleigh fractional crystallization, which can be described by Eq. 1,
613 log(K/Rb) and log(Cs) define a linear relationship (Eq. 3). The slope of this line (*m*) is
614 defined by the bulk partition coefficients *Dj* for each element *j* (Eq. 4) and its intercept (*b)*
615 depends on the starting composition of the melt as well as the partition coefficients $k_{j,i}$
616 between mineral *i* and melt (Eq. 5).

617 Assuming closed system Rayleigh fractional crystallization for the studied pegmatite
618 and applying the approach of Hulsbosch et al. (2014) to each zone identified in the
619 concentration profile of muscovite LB-A-Ms-2 (Figs. 8 and 11), we can estimate the bulk
620 partition coefficients D_j as well as the starting composition $C_{0,j}$ (j = K, Rb and Cs) of the
621 evolved melt by varying these until Eqs. 4 and 5 match *m* and *b* from linear regression of the
622 empirical data. Furthermore, the distance *z* along the profile of the concentration
623 measurements correlates to the amount of remaining melt *F*, assuming constant ratios
624 between growth rates of the different minerals taking up the elements of interest.

625 Figure 14a shows log(K/Rb) and log(Cs) for zone I.3 in the direction B–A (Fig. 8).
626 This direction was chosen, because it is parallel to the cleavage, the direction of fastest
627 crystallization, and should therefore yield the highest resolution. The data define a linear
628 trend with $m_{I.3}$ = -0.361 and $b_{I.3}$ = 2.304 (Fig. 14a). The following constraints were used to
629 approximate the bulk partition coefficients: concentrations of Rb and Cs increase, which
630 suggest that these elements behave incompatibly and therefore $D_{Rb} < 1$ and $D_{Cs} < 1$, while K
631 shows a slight decrease, which is best approximated by $1.00 < D_K < 1.01$. Published data for
632 muscovite/melt partition coefficients (Table 5) were used for calculating the intercept. An
633 approximate starting composition for the evolved melt from which muscovite LB-A-Ms-2
634 crystallized can be inferred by solving Eq. 2 for $C_{0,}$ and assuming that the average of the first
635 few points of the profile represents the starting composition of the mineral at $F \approx 0.99$. It is
636 then possible to model the concentration of Cs, K and Rb in the crystal for $1 > F > 0$ by using
637 the approximated bulk partition coefficients and starting composition to solve Eq. 2. The
638 linear relationship of distance *z* with log(Cs) (Fig. 14b, R^2=0.814) can then be used to fit the
639 modeled concentrations to the observed profile. After fitting the modeled concentrations,
640 partition coefficients for Nb and Ta were inferred from the trends observed in the respective

profile. The profiles for I.3 with the modeled concentrations for Cs, Rb and Nb obtained with three different D_j values each are shown in Fig. 14c.

The same approach was used to model zones II.1, II.2, II.3, III.1 and III.3. Melt compositions at the start of crystallization and at the end of each zone, *m* and *b*, as well as bulk partition coefficients for each zone are shown in Table 6. The bulk partition coefficients yielding best results for *m* and *b* do not always resemble the actual concentration trend for K and Rb observed in the profile and the values in parentheses in Table 6 are for bulk partition coefficients that best approximate K and Rb behavior. The melt compositions at the end of crystallization are more similar to the starting composition for the subsequent zone for these bulk partition coefficients, and *m* and *b* are more similar to the slope and intercept of zone I.3. The starting and end concentrations of each zone yield additional information: zone I.3 gets strongly enriched in Cs towards the end, while the initial melt concentration of zone II.1 is lower. As there is no mineral with Cs compatibility crystallizing, Cs must be removed from the crystallizing medium another way, or the crystallizing medium must have changed. Potassium behaves compatibly for all zones ($D_K > 1$) apart from II.2, but the starting concentrations of K in the melt only decrease from I.3 to II.2 and increase with II.3. Between stages II and III, another Cs-loss event accompanied by strong increase in K/Rb is observed. In zone III.2, Cs and Ta are highly compatible with bulk distribution coefficients of 5.25 and 3.20, respectively.

Bulk partition coefficients are the sum of mineral/melt partition coefficients (Table 5) multiplied by the mineral fraction. This relationship allows constraint of the proportions of the crystallizing minerals, which was undertaken for the individual zones and is described in Supplementary Note C. Good results fitting bulk partition coefficients of *Dj* (*j* = K, Rb, Cs) were achieved for crystallization of muscovite (±albite, quartz) in the presence of an aqueous medium with oscillating proportions of the latter during stage II. Spreadsheets including the raw data and geochemical models for each zone can be found in supplementary file ST3.

$$\frac{C_{liq,j}}{C_{0,j}} = F^{(D_j-1)} \qquad \text{(Eq. 1)}$$

$$C_{i,j} = C_0 \times k_{d,i,j} \times F^{(D_j-1)} \qquad \text{(Eq. 2)}$$

$$\log\left(\frac{C_{i,K}}{C_{i,Rb}}\right) = m \times \log\left(C_{i,Cs}\right) + b \qquad \text{(after Hulsbosch et al., 2014)} \quad \text{(Eq. 3)}$$

$$m = \frac{D_K - D_{Rb}}{D_{Cs} - 1} \quad \text{(Eq. 4)}$$

$$b = \log\left(\frac{C_{0,K} \times K_{d,i,K}}{C_{0,Rb} \times K_{d,i,Rb}}\right) - m \times \log(C_{0,Cs} \times K_{d,i,Cs}) \quad \text{(Eq. 5)}$$

With

F: mass fraction of residual melt;

$C_{0,j}$: initial melt concentration of element j at $F = 1$;

$C_{liq,j}$, $C_{i,j}$: concentrations of element j in residual melt and in mineral i at F;

$k_{d,i,j}$: partition coefficient for element j between mineral i and liquid, $k_{d,i,j} = \frac{C_{i,j}}{C_{liq,j}}$

D_j: bulk partition coefficient for element j, $D_j = \sum_i X_i \times k_{d,i,j}$

X_i: mass fraction of mineral j, $\sum_i X_i = 1$.

6.2.2. Rare-element fractionation

To investigate the fractionation behavior and correlation of rare elements in all muscovite samples, the data was plotted on fractionation plots (Fig. 15). For stages I and II, concentrations of Li and Cs clearly increase with decreasing K/Rb and patterns similar to that of Cs (Fig. 15a), but with a greater scatter at lower K/Rb, are observed for Sn and Nb (not shown). The arrows in the K/Rb–Cs plot show the modeled concentration changes from start to end of the profiles across muscovite LB-A-Ms-2. The trends of stages I and II in LB-A-Ms-2 define a field which includes almost all measurements. The apparent Cs-loss after stages I and II (section 6.2.1) can be observed in this plot: Stage II starts at almost the same K/Rb as the end of stage I, but the Cs concentration is comparable to the starting concentration of zone I.3, while stage III starts at even lower Cs as well as higher K/Rb. The trend for zone III.1 can still satisfactorily be explained with fractional crystallization, but III.2 shows a reversed trend.

For Ta/Nb, the behavior seems erratic, but the trends modeled for the zones in LB-A-Ms-2 (Fig. 15a, arrows) seem to explain well the behavior in the other grains at low K/Rb. Behavior at high Ta/Nb and high K/Rb, observed for stage III, seems more complex. Similar behavior is also observed for Ti in relation to K/Rb (not illustrated). However, compared to B, anti-correlation is visible for Ta/Nb (Fig. 15b) and Ti (not illustrated). A strong correlation of Mn and Li is observed, with two opposite trends for the two lithologies (Fig. 15b). The high-Li central samples (QM-A) increase in Li and Mn from stage I to stage II, while the low-Li, border samples decrease in both elements from stage I to stage II. Similarly, two trends with opposite slopes were observed for Li vs Ta/Nb (Fig. 15b, dashed lines).

The outermost muscovite zones, which crystallized during stage III, show high K/Rb ratios combined with intermediate to low rare-element concentrations (Fig. 15). Consequently, fractionation in terms of K/Rb (and K/Cs) is reversed towards the end, which means that either less rare-elements are available in the crystallizing medium, or that the system was flooded with K (or both). Apart from that, stage III muscovite still has high Ta/Nb (Fig. 15b), with intermediate Ta and Nb of ~50–100 ppm and ~60–120 ppm, respectively.

Barium (not illustrated) seems to slightly decrease with decreasing K/Rb for stages I and II, as lowest Ba concentrations are found at low K/Rb, but the scatter is large and high Ba concentrations at low K/Rb are particularly common in stage II. Behavior of Be, Ga, and Zr/Hf is briefly described in Supplementary Note B.3.

7. Discussion of zoning and rare-element fractionation

Zoning (including oscillatory zoning) of white mica has been described in the Leinster Batholith (Roycroft, 1991), S-type granites in northern Portugal (Gomes and Neiva, 2000) and Nova Scotia, Canada (Clarke and Bogutyn, 2003), as well as granitic pegmatites in Namibia (Roda-Robles et al., 2007). These studies document white micas which are zoned in major elements; are macroscopically zoned, or show zoning by epitactic overgrowth of different mica species. Only Clarke and Bogutyn (2003) provide *in-situ* trace element data, but with low spatial resolution. While major-element zoning of white mica is common, muscovite in our study is homogenous in its major-element composition within the analytical precision of SEM-EDS. The homogeneity is evident from the lack of optical zoning (macro- and microscopically), homogenous BSE intensities and low standard deviations for average concentrations of K, Al and Si as determined by SEM-EDS. However, high-resolution LA-ICP-MS imaging demonstrated that minor and trace element concentrations vary strongly over several growth zones.

Studies on minor- and trace-element zoning in white mica from granites and pegmatites are sparse. Viana et al. (2007) present chemical data for a single muscovite megacryst (40x80 cm) from a rare-element pegmatite from the Eastern Pegmatite Province in Minas Gerais, Brazil. Again, spatial resolution was low: samples were analyzed using X-ray fluorescence spectrometry on subsamples with 30 mm diameter. The authors conclude that the observed zoning is mainly caused by hydrothermal alteration because of depletion of elements such as Rb, Ga, Y, Nb, Ta, and Sn towards a large fracture crosscutting the crystal

and the origin of the primary zoning is uncertain. Tantalum, Nb and Sn seem to correlate to Rb in the study of Viana et al. (2007), but not in the present study.

Muscovite forming contemporaneously with, or after crystallization of, CGM and after alkali feldspar in the Moose II LCT pegmatite was described by Anderson et al. (2013). However, compared to the present study, concentrations of Li, Rb and Cs in muscovite were an order of magnitude lower and no clear intra-grain zoning was observed. Nevertheless, the authors describe strong enrichment of Cs and Rb at the margins of most grains, which are attributed to late-stage reaction processes, rather than primary fractional crystallization.

Most trace element variations observed in the present study correspond well to published bulk data for mica in spodumene pegmatites (e.g. Černý and Burt, 1984), except for barium. In granitic melt systems, Ba is expected to decrease with increasing magmatic fractionation (i.e. increasing K/Rb) due to fractional crystallization of alkali feldspar, which was also observed for a large mica dataset for rare-element pegmatites (Černý and Burt, 1984). Nevertheless, in the present study, an increase in Ba towards the outer zones is observed along with an increase in K/Rb and K/Cs and therefore magmatic fractionation trends are reversed. A potential source for Ba and K in the border albitites is discussed below (6.3.3).

Modeling of Rayleigh fractional crystallization showed that the strong Cs-enrichment at the end of stage I observed in I.3 for muscovite LB-A-Ms-2 requires the Cs concentration in the melt to reach weight-percent levels (Table 6). London et al. (1998) reported that saturation for pollucite ($CsAlSi_2O_6$) in H_2O-saturated haplogranitic melts is reached at ~4.7 wt% Cs at 200 MPa and 680 °C. This is an extreme enrichment compared to the average crustal abundance of 2 ppm Cs (Linnen et al., 2012), but not compared to ~1 wt% Cs observed here. Furthermore, a review of the temperature dependence of pollucite solubility in London (2005) proposes that Cs-saturation is reached at ~0.47 wt% Cs at 390 °C. However, the effects of increasing peraluminosity and concentration of network modifiers (including H_2O) were not addressed in these studies. In natural systems, pollucite precipitation might also be influenced by these factors.

Pollucite has not been detected in the Leinster LCT pegmatites, probably because Cs-concentrations were not high enough in earlier stages of pegmatite formation. For the Tanco pegmatite, Manitoba, Canada, the starting concentration of Cs was high and Cs-saturation might have already been reached after 40–50% solidification of the pegmatite-forming melt (London, 2005). Published bulk compositions for rare-element pegmatites at Aclare

(O'Connor et al., 1991; Barros and Menuge, 2016) yield 63–77 ppm Cs. If this concentration represents the actual starting concentration of rare-element pegmatite melt, this melt would have to crystallize to more than 99% to produce the Cs enrichment observed in our samples. Therefore, Cs saturation would only be attained at the very end of solidification if closed-system fractional crystallization is the only process by which Cs is enriched. However, fractional crystallization to such a high degree seems unlikely, as H_2O saturation in the silicate melt was probably reached earlier. This saturation would cause the release of an aqueous medium, influencing the distribution of Cs and other incompatible elements (see below).

In the following subsections, we propose a crystallization model (6.3.1), which is then discussed in the context of replacive albitite (6.3.2) and quartz–muscovite (6.3.3) crystallization. Rare-element fractionation patterns, partition coefficients, element solubilities and the observed differences between the individual stages, will be assessed to distinguish between crystallization from *silicic melt*, from *aqueous melt* or from *hydrothermal fluid*. The three terms will be used in accordance with recent literature (Thomas and Davidson, 2013, 2016) as follows: *silicic melt* for silicate-dominated volatile-bearing peraluminous melt; *aqueous melt* for a H_2O-dominated alkaline and depolymerized fluid phase at magmatic temperatures (which shares characteristics with a silicic melt and supercritical fluid); and *hydrothermal fluid* for a supercritical saline (F-Cl-enriched) H_2O-dominated phase with low silica content and abundant network modifiers like C, S, B and P. All three phases are assumed to be immiscible with each other and may coexist. *Medium* is used as a generic term, which can refer to any of the three phases.

7.1.1. Late crystallization from coexisting melts and saline fluid

Recent studies (Thomas and Davidson, 2016, and references therein) on fluid and melt inclusions and melt–melt–fluid immiscibility show that parental pegmatite melts might initially start as supercritical melts with complete miscibility of aqueous and silicic endmembers. Full miscibility for these endmembers in Na-, B- and P-rich systems was also experimentally demonstrated by Sowerby and Keppler (2002) and those authors concluded that a combination of network modifiers could move the critical curve to moderate P–T conditions plausible for pegmatite emplacement. After cooling below the critical temperature of ~720 °C (Thomas and Davidson, 2016), two immiscible phases coexist, a volatile-rich silicic melt (with up to 30 wt.% H_2O) and an aqueous depolymerized melt (referred to as

"fluid/melt" by Thomas and Davidson, 2016). Furthermore, hydrothermal fluid (or vapor) is released, while the system progresses from being melt-dominated to completely hydrothermal.

The apparent Cs-loss between stages I and II (Table 6; Fig. 15) can be explained by crystallization from Cs-poorer aqueous melt coexisting with silicic melt. Hydrothermal fluid, if released early, might also remove part of the Cs from both melts. The fluid/melt partition coefficient for Cs used for modeling in the present study (0.5, Jolliff et al., 1992) predicts compatibility of Cs in silicic melt, but fluid/melt partition coefficients for Cs as high as 7–23 with decreasing pressure from 200–50 MPa in a Cl-F-rich system of hydrothermal fluid and high-silica melt were reported by Webster et al. (1989).

Zoning for the other elements observed in our muscovite samples can also be explained by a shift from – or by an oscillation between – crystallization from silicic melt to crystallization from H_2O-dominated media. We therefore propose that stage I zones crystallized from a silicic melt and that the transition to stage II marks the end of pure magmatic crystallization, with probable exsolution of a saline hydrothermal fluid besides coexisting aqueous and silicic melts. During stage II, crystal growth oscillates between crystallization from an aqueous melt (II.1 and II.3) and crystallization from a silicic melt (II.2). At the same time, both media become enriched in network modifiers such as B, F, P due to ongoing fractional crystallization. In stage III, crystallization from the last silicic melt is observed. After III.1, the saline hydrothermal fluid causes hydrothermal alteration, overprint and formation of zones III.2 and III*. This sequence is supported by the following observations:

- Stage I shows behavior of K, Rb, and Cs (Figs. 10a, 11 and 15) which is in good agreement with magmatic Rayleigh fractional crystallization, while in models for stage II, the bulk partition coefficients for K and Rb either do not match the observed concentration profile or they do not match slope and intercept for log(K/Rb) versus log(Cs) (Table 6). However, general trends for K/Rb and Cs (Fig. 15) in white mica can still be explained by fractional crystallization until zone III.2. Afterwards, the trends are reversed and precipitation happens by another process.
- Embayment textures often observed between zones of stages I and II (muscovite: Figs. 6–8; CGM: Fig. 4) suggest a petrogenetic gap and possible partial digestion of earlier zones. Additionally, the zones of stage II, which crystallized from

aqueous melt, show irregular (but not necessarily truncated) borders, while the zones generated from silicic melt at the same stage show straighter, sub- to euhedral borders.

- Boron is low in the silicic melt zones and high in zones potentially produced by precipitation from aqueous melt (Fig. 10b). It is also high in fine-grained hydrothermal epitactic mica (III.2). Boron typically partitions into aqueous media in coexistence with a silicic melt (Thomas et al., 2003, and references therin).
- Most HFSE are enriched progressively towards the end of stage I (Fig. 10b), which is in agreement with behavior of incompatible elements during magmatic fractional crystallization. During stage II, behavior seems erratic with sudden depletion or enrichment, requiring a change of the crystallization medium, which is further investigated below.

Studies on natural fluid inclusions and experimental systems (e.g. Veksler, 2005; Rickers et al., 2006; Hulsbosch et al., 2016; Thomas and Davidson, 2016) showed that Li, Be, B, Na, P, Zr, Nb and W favor depolymerized alkaline aqueous melts, while Rb, Cs, Hf and Ta partition into silicic melt. Both phases become enriched in F due to fractional crystallization (Veksler, 2005). Most of this is in agreement with our observations for stage II: High-B, low-Ta/Nb (i.e. Nb-enriched) muscovite crystallizes from aqueous melt, while low-B, high-Ta/Nb, high-Cs muscovite crystallizes from silicic melt. High W in the magmatic zone of stage II of muscovite LB-A-Ms-2 seems contrary to the aforementioned partition behavior. However, absolute concentrations of W in the mica are low (< 8 ppm) and the behavior can be explained by higher compatibility of W in muscovite compared to the silicic melt from which it is crystallizing. This zone shows also high Sn concentrations. The behavior of Sn is not well constrained in the literature: in an experimental F-rich H_2O–melt system, Sn favors silicic melt, while in B- and P-rich H_2O–melt systems, Sn partitions into the aqueous medium (Thomas et al., 2003; Veksler, 2005). Tin favoring the silicic melt over aqueous media is also the conclusion of several experimental studies reviewed by Linnen and Cuney (2005). However, these authors propose that Sn partitions into hydrothermal fluid at high Cl concentrations, which might also happen at higher F concentrations. The effect of the oxidation state of Sn was furthermore not investigated in these studies. In our samples, Sn seems to favor silicic melt and strongly partitions into the growing muscovite (with up to 1000 ppm Sn). This compatibility suggests that tetravalent Sn is present, as it has a similar

ionic radius to other elements compatible with the octahedral site of white mica. Titanium exhibits similar behavior to Sn and Ta and is probably controlled by similar processes.

Behavior of Nb and Ta in white mica seems to be in disagreement with Rayleigh fractional crystallization even during stage I (arrow in Fig. 15). However, our geochemical modeling did not consider fractional crystallization of CGM, which helps to explain the distribution of these elements in muscovite. Zoning observed in CGM fits well into the sequence of crystallization from coexisting silicic and aqueous melts towards hydrothermal fluid described above as well as the bulk partition coefficients derived from geochemical modeling.

Crystallization of CGM starts in stage I and continues until stage III, which is recorded by CGM inclusions associated with zones I.3 and III.1 of muscovite in border albitite samples, as well as the correlative Ta#-patterns of muscovite and CGM in the lower border albitite sample (Fig. 13). CGM zones of stage I are rich in HFSE (Ti, Sn, W, U) and exhibit increasing Mn# and decreasing Ta# from their centers to their rims. Increasing Mn# is expected for magmatic fractional crystallization as observed in many other highly fractionated pegmatites globally (e.g. Lahti, 1987; Mulja et al., 1996; Wise et al., 2012; Badanina et al., 2015). High U-contents and uraninite inclusions are also consistent with crystallization from silicic melt, where CGM can incorporate high amounts of U and commonly show exsolution of uraninite after cooling (Romer and Wright, 1992). Decreasing Ta#, referred to as reversed zoning by Lahti (1987), is inconsistent with the expected magmatic trend of increasing Ta# predicted by columbite–tantalite solubility experiments (see Linnen and Cuney, 2005, and references therin). Reversed zoning of CGM in our example is likely caused by contemporaneous crystallization of white mica and CGM, and probably also by the presence of coexisting aqueous media. Muscovite/melt partition coefficients for Nb and Ta of 3.5 and 0.42, respectively, for a Li-F-P-rich peraluminous rhyolite presented by Raimbault and Burnol (1998), suggest strong compatibility of Nb, but incompatibility of Ta, in muscovite. While Nb should still be more compatible in CGM compared to muscovite, the volume of newly-formed mica is much larger than the volume of crystallizing CGM. Additionally, Nb is more susceptible to partitioning into a coexisting fluid while Ta remains in the melt as described above.

After stage I, CGM are partially resorbed as evident by truncation and crosscutting of stage I zoning patterns (Figs. 4 and 5). This is followed by growth of Nb-rich (low-Ta#) CGM from an aqueous melt phase, which is in good agreement with the high bulk partition coefficients for Nb during growth of muscovite zones II.1 and II.3 (Table 6). The silicic melt-

related growth during muscovite zone II.2 is associated with high-Ta# CGM and strong incompatibility of both Nb and Ta in the system. Tantalum has a very low bulk partition coefficient in II.2 suggesting high compatibility in the crystallizing medium. Partial resorption can be explained with increasing Li and F in the liquids. Both elements possibly increase the solubility of CGM in silicate melts (Linnen and Cuney, 2005).

Decrease of Mn# during stages II to III, followed by an increase, is observed in the EDS profile of CGM-1 (Fig. 5). The decrease might be linked to crystallization of Mn-rich F-apatite and lithiophilite, which is in agreement with petrographic observations. The steep increase in Mn# at the end might mark the termination of phosphate crystallization. Trace elements (especially U) are also depleted at the beginning of stage II, but increase again towards stage III. Texturally, each high-Ta# zone in CGM-1 shows subhedral boundaries, but also common textures of partial digestion. For the other two CGM, textures are more complex (Fig. 4b–c). Correlation of the zones showed that the high-Ta# part of stage II in CGM-3 is not a Ta-rich overgrowth, as observed in the other grains, but replacement of the Nb-rich zone II.1 by the high-Ta# zone II.3, which agrees with the texture observed on the BSE image.

The crystallization history of CGM can be explained analogously to that of muscovite. At stage I, CGM crystallize from a silicic melt; stage II is characterized by partial digestion, replacement, and crystallization from two different melts (low-Ta/Nb aqueous melt and high-Ta/Nb silicic melt); and in stage III high-Ta# CGM grow from the remaining melt. Furthermore, geochemical modeling for muscovite showed that the vapor, which deposits the epitactic mica (III.2) at the end of mica crystallization, is highly enriched in Ta compared to Nb (180 ppm and 29 ppm, respectively). Bulk partition coefficients are large for both elements (Table 6), but D_{Ta} is >2 times D_{Nb}. The reason for this fractionation could be strong F-enrichment towards the end. Experimental work shows that F might increase the solubility of both Nb and Ta in silicate melt (Keppler, 1993), but more recent experiments document no significant influence of F (Fiege et al., 2011; Aseri et al., 2015). Either way, fluorine has little effect on the Ta/Nb ratio of silicate melts (see also Linnen and Cuney, 2005). In contrast, different stabilities of Ta- and Nb-F-complexes in Na-, Cs-, Rb-bearing aqueous solutions have been exploited for hydrometallurgical separation of Ta and Nb for over 150 years (e.g. Smith, 1905). In these processes, separation is possible because, compared to Nb, Ta forms more stable (and more mobile [Parker and Fleischer, 1968]) fluoro-complexes in aqueous solution.

A similar process of late-magmatic crystallization of mica was observed by Clarke and Bogutyn (2003) for the South Mountain leucogranite in Nova Scotia. They infer the origin of mica cores as precipitates from silicic melt, while mica rims are interpreted to have formed late in the presence of a hydrothermal fluid. The epitactic rims also correlate locally with hydrothermal alteration and aplite–pegmatite–greisen formation (Clarke and Bogutyn, 2003). The authors furthermore observed crystals where fluid-related growth was followed by magmatic growth, followed by more fluid-related growth. These oscillations are interpreted as crystallization during changing *P–T–x* caused by periodic build-up and release of an aqueous phase. However, the published work on melt–melt–fluid immiscibility in granites and pegmatites referenced above, suggests that silicic and aqueous media might actually coexist without a need for periodical influxes.

7.1.2. Formation of albitite

Fine-grained albitites are widely regarded to appear late in the pegmatite-forming process. They are generally considered as replacement units and are the main host for economic Nb–Ta mineralization. Kontak (2006) proposes that secondary albite in the Brazil Lake pegmatites of Nova Scotia formed by direct alkali-ion exchange between Na-rich *melt* and alkali feldspar megacrysts. While the Brazil Lake pegmatites are compositionally and geologically similar to the Leinster rare-element pegmatites, it is unlikely that this process happened in the Leinster pegmatites. Albitite is abundant (up to 15%) in the studied drill core and at other localities in the Leinster pegmatite belt. Furthermore, it is often not associated with remnant alkali feldspar suggesting it either can form without any alkali feldspar present or that the replacement of alkali feldspar was close to 100%. While formation of late-stage (or secondary) muscovite is common (see 6.3.3.), it might not account for all released K if all secondary albite replaced alkali feldspar. Furthermore, if albite formed by direct alkali-ion exchange of alkali feldspar with a Na-rich medium, we would expect pseudomorphic replacement of alkali feldspar by albite and diffuse grain boundaries or intimate intergrowth between the reactant and product, which was not observed here. Moreover, experiments and natural examples demonstrate that alkali feldspar replacement during such a reaction is topotaxial and produces a common crystal orientation of secondary albite grains (e.g. Holness, 2003; Norberg et al., 2011), again not observed here.

The small grain size and low size variation of albite crystals indicate a high nucleation rate. Additionally, the common alignment of the lath-shaped and platy albite crystals parallel to the pegmatite margin suggests crystallization from a flowing liquid. These observations

971 point towards sudden crystallization from a mobile medium, which was migrating through
972 the pegmatite body. Rapid nucleation of albite within a residual Na-rich magmatic liquid
973 might be explained by a sudden pressure drop after release of a vapor phase and transitioning
974 from lithostatic to hydrostatic pressure, or by an increasing solidus temperature due to
975 fractional crystallization of flux-bearing (Li, B, F, P) minerals (London, 2014). Neither
976 hypothesis explores the possibility of albite precipitation from a silica-bearing hydrothermal
977 fluid, which is an established mechanism for albite precipitation during albitization of
978 granitic rocks (e.g. Holness, 2003; Plümper and Putnis, 2009; Putnis and Austrheim, 2010).
979 The euhedral to subhedral shape of the outer zones of CGM within lower border
980 albitite suggest that albite crystallization did not commence before, or at least was still
981 ongoing, during stage III. This is also in agreement with petrographic observations as albite
982 laths truncate stage-II and -III trace-element zoning in muscovite LB-A-Ms-2 (Fig. 8). Direct
983 association of stage-III zones in LB-A-Ms-2 with remnant microcline suggests replacement
984 of microcline by muscovite via dissolution–precipitation along the grain boundary interface.
985 Microcline was dissolved and the stage-II muscovite provided a nucleation surface for
986 precipitation of stage-III muscovite. However, dissolution of microcline might have started
987 earlier causing flooding of the system with the network formers Al and Si, which could
988 explain alternation between crystallization from aqueous melt and crystallization from silicic
989 melt during stage II.
990 Embayment and truncation of the early muscovite and CGM zones, potentially caused
991 by an aggressive F-rich magmatic medium, makes contemporaneous dissolution of
992 microcline furthermore plausible. However, the K/Rb ratios of crystallizing liquid and
993 muscovite still decrease until the end of stage II. In stage III, a bulk K partition coefficient of
994 0.76–0.85 suggests K-enrichment of the liquid, which is caused by microcline breakdown. It
995 is also reasonable to consider fractional crystallization of albite as cause for a bulk K partition
996 coefficient <1, but no feasible solution of the model for III.1 yields high proportions of albite.
997 If K is not partitioning into a vapor phase (which might not yet be involved in crystallization
998 during stage II), significant dissolution of microcline might not occur until very late, but still
999 before precipitation of albite. In our model, no melt is present after crystallization of zones
1000 III.3, but mica textures suggest that dissolution of silicates continues. This might alter the
1001 chemistry of the residual fluid by depleting the liquid in reactive species like F, and by
1002 increasing its pH through hydrolysis of silicates. Eventually, these chemical changes would
1003 shift the liquid into the stability field of albite, followed by sudden albite precipitation. This
1004 hypothesis is in agreement with studies on feldspar replacement reactions in granitic rocks

(e.g. Wibberley and McCaig, 2000; Plümper and Putnis, 2009). These studies present thermodynamic models for albite–K-feldspar–white-mica phase equilibria as a function of Na^+ and K^+ activity over H^+ activity (Fig. 1 in Wibberley and McCaig, 2000). An increasing pH shifts the system into the feldspar stability fields and albite precipitates when $a_{Na} > a_K$. Furthermore, the resulting white mica instability is consistent with the breakdown of muscovite described above.

Minute apatite inclusions in albite (Fig. 3f) indicate that albitization is accompanied by F-apatite precipitation, which is also in agreement with an increasing pH (e.g. Ayers and Watson, 1991). Phosphorous and Ca content of the liquid are probably high in the first place, due to absence of Ca- or P-bearing minerals during fractional crystallization. Additionally, breakdown of P-rich microcline released additional P and Ca, potentially contributing to apatite saturation.

The porosity of albite crystals, the sharp grain boundaries between albite and remnant muscovite and microcline, as well as the co-precipitation of other phases (here F-apatite) are characteristics indicative of hydrothermal feldspar formation (Plümper and Putnis, 2009; Putnis and Austrheim, 2010). Furthermore, albite precipitation from a peralkaline, halogen-rich hydrothermal fluid is in agreement with fluid inclusion analyses of Barros (2017), who reports high salinity (>20 eq. wt.% NaCl) and homogenization temperatures of 250–300 °C for fluid inclusions associated with albitization at Aclare.

After albite precipitation, Na^+ activity is strongly diminished, eventually leading to white mica stability. The residual liquid or vapor causes formation of fine-grained hydrothermal epitactic muscovite (III.2, Fig. 3g), formation of secondary minerals, as well as replacement of muscovite by BSE-bright Li-F-Mn-Cs-rich mica (III.*; Fig. 3d–e). The secondary fine-grained muscovite intergrown with quartz and replacing microcline along fractures (Fig. 3f) is probably also derived from this vapor. The fractures only rarely extend into albite and such alteration of albite is mainly observed along grain boundaries shared with microcline. This suggests that the release of the hydrothermal vapor is associated with a change of the stress field, which caused hydraulic fracturing while albite was still precipitating. In upper parts of the pegmatite, sub-vertical fractures and veins with mica and quartz crosscut the rock. This fracturing might have been caused by the fluid which migrated through the pegmatite towards the headwall.

7.1.3. Formation of quartz–muscovite assemblages by hydrothermal replacement

White mica of the quartz–muscovite assemblage formed during stage II. The elongate habit of core zones in QM-A-Ms-2 (Fig. 7) suggests that this mica might have initially formed as a sericitic-like alteration of primary feldspar by an F- and rare-element-rich aqueous medium. Further alteration led to near-total replacement of pegmatitic alkali feldspar by muscovite and quartz. Pyrite and chalcopyrite are also common in the quartz–muscovite assemblage, which is typical of phyllic alteration. The high Li-concentration in QM-A (Fig. 10a), replacement of spodumene by white mica in other parts of the drill core, as well as common Li-phosphates in adjacent albitite, all suggest that spodumene was also replaced.

Beryl and garnet are probably remnants of the early pegmatite assemblage. Beryl is strongly altered as evident by irregular grain boundaries and fractures often filled with Mn-rich calcite or apatite. Garnet is associated with alteration to BSE-bright Li-Mn-Cs-rich mica along fractures and grain boundaries. The only other remnants of stage I minerals are cores of white mica between the quartz-muscovite assemblage and adjacent albitite (QM-A-Ms-3).

Volumetrically, most of the mica crystallized late during stage II and mainly in stage III, as indicated by the correlation of mica growth zones. This late formation helps to explain the interfingering of albitite and QM-A: if albitite formed from hydrothermal fluid released late in stage II, or at the beginning of stage III, this fluid must have been immiscible with the medium producing QM-A. Direct exsolution of the albitite-forming fluid from QM-A towards the end of quartz–muscovite crystallization also seems plausible.

8. Implications for rare-element pegmatite crystallization

8.1. Stages of Leinster rare-element pegmatite formation

The three stages of rare-element pegmatite formation from our model are summarized in the following subsections and Fig. 16. The paragenetic sequence over these stages is illustrated in Fig. 17.

8.1.1. Stage I – Magmatic crystallization and exsolution of aqueous liquids

Stage I marks the end of pure magmatic crystallization and transition to a magmatic–hydrothermal stage II (Fig. 16a). Stage I is characterized by progressive enrichment of the melt in rare elements due to fractional crystallization of primary pegmatitic alkali feldspar, plagioclase, muscovite, quartz, spodumene, accessory beryl and garnet, and later columbite–

tantalite. An immiscible aqueous melt might already coexist at this stage, as suggested by fluid inclusion work for other localities, but no evidence was found in muscovite or CGM in the present study. During this stage Ta# is mainly increased by fractional crystallization of muscovite. At the end of stage I, the melt is also enriched in Ti, W, Sn, and U, as recorded by high concentrations of these in stage-I CGM.

8.1.2. Stage II – Magmatic–metasomatic crystallization

Stage II is characterized by onset of crystallization from aqueous melt (Fig. 16b). The degree of fractionation (as expressed by decreasing K/Rb) increases only slightly, while highly incompatible Cs reaches its maximum concentration during the silicic melt-related growth of this stage. Muscovite crystallizing from aqueous melt is especially richer in B and Nb compared to muscovite crystallized from silicic melt, while the latter shows enrichment especially in Ta and Sn.

Stage II also records the onset of metasomatic replacement of stage-I silicates by muscovite and quartz, as well as partial dissolution of primary pegmatite minerals including CGM. Resorption is likely caused by elevated reactivity of the liquids, especially due to F-enrichment (but also Li-B-P-enrichment) during fractional crystallization. Cesium concentrations of the crystallizing liquids are lower than expected after stage I as well as after the end of stage II. Besides Cs partitioning between the two melts, this could be explained by exsolution of a third liquid: an aqueous, halogen-rich, supercritical fluid, which removes part of the alkali metals from the other two liquids (Fig. 16c). Crystallization of muscovite further increases Ta# of remaining liquids. Partitioning of HFSE between melt, fluid, muscovite and CGM causes oscillating concentrations of these elements in stage II zones. The fluid pervades the almost solidified pegmatite body along grain boundaries and pathways created by partial resorption. Transition to a hydrostatic pressure regime causes hydraulic fracturing, creating additional pathways. Partial digestion also remobilizes elements such as Al and Si, which might generate polymerized media locally.

8.1.3. Stage III – Last melt and hydrothermal precipitation

In stage III, final crystallization from melt is observed and is accompanied by further breakdown of microcline. The last melt is highly enriched in HFSE and has an extreme Ta# of ~0.8, while concentrations of Cs and Rb drop. The latter is probably caused by dilution with K released from microcline, as well as partitioning of rare alkali metals into aqueous, now highly B-F-P-enriched, fluid. During solidification of the last portions of melt, the

remaining incompatible elements are increasingly absorbed by the saline hydrothermal fluid, leading to secondary overgrowth and formation of hydrothermal minerals. This highly reactive fluid causes (F-catalyzed) hydrolysis of earlier silicates, which eventually leads to precipitation of albite (and F-apatite) due to changing pH. During and after precipitation of albite the residual fluid migrates through the pegmatite body (Fig 16d) causing hydraulic fracturing and hydrothermal mineral precipitation including partial replacement of muscovite by Li-F-Mn-Fe-Cs-rich mica. Finally, the remaining vapor may leave the dike, as the volumetric proportion of hydrothermal rare-element-bearing minerals is low and prominent rare metal and B halos develop around these pegmatites (Barros, 2017).

8.2. Consequences for Nb–Ta mineralization

Crystallization of CGM started late in the primary magmatic evolution of the Leinster LCT pegmatites (Fig. 17). Perfectly euhedral crystals with normal zoning, and in sharp contact with other minerals, were not observed. High Ta# in CGM cores and reversed zoning suggest crystallization from a melt, whose Ta/Nb was already increased by fractional crystallization of muscovite. Columbite group minerals are mainly observed in the low-Li parts, which are associated with primary alkali feldspar, quartz and plagioclase. Higher CGM solubility at high Li concentrations of silicate melts (Linnen, 1998) impedes CGM crystallization before crystallization of spodumene. Nevertheless, even at the final stages, Nb and Ta concentrations of melt were far below their (F- and Li-dependent) experimental saturation thresholds of 70–490 ppm Nb and 510–6800 ppm Ta (Linnen and Cuney, 2005). Early CGM might form as inclusions in large silicate crystals, where they crystallize from an enriched boundary layer melt at the advancing crystallization front of the growing silicate (c.f. Fenn, 1986). In Leinster pegmatite samples, CGM inclusions can be found in alkali feldspar and muscovite. The cores of the analyzed CGM might be relics of microcline inclusions, which would add another constraint to the timing of onset of microcline dissolution (6.3.2). Relic grains inherited from replaced pegmatite units have been postulated for primitive CGM in albitites of rare-element pegmatites elsewhere (e.g. Novák et al., 2003; Wise and Brown, 2011). Stage I CGM zones were partly resorbed, overgrown or replaced during stage II. The rather low concentrations of Ta and Nb combined with high F concentration in the fluids make resorption likely. Crystallization might have been feasible nevertheless, because the earlier cores served as nucleation sites. Epitaxial crystal growth on an isomorphic substrate from undersaturated solutions was described by Murdaugh et al.

(2007) who propose that the substrate (in this case, stage I CGM) interacts with the liquid by attracting the solubilized species (Nb, Ta complexes in the melt), which creates local supersaturation followed by crystallization (of stage-II CGM) on the surface of the substrate. Repetition of this process might also generate small-scale oscillatory zoning, as only thin crystal layers are produced during one iteration.

The early magmatic CGM can show high Ta#, which would make them economically interesting. The main phases of Ta precipitation are melt-dominated phases of stages II and III as well as the late hydrothermal phase where the highest-Ta minerals are formed. Van Lichtervelde et al. (2009) interpret crystallization of late (or secondary) Ta phases such as late CGM and microlite as products of Ta remobilization during formation of secondary mica. This might only be partly true, as the late fluids appear already enriched in Ta compared to Nb due to muscovite crystallization. However, common embayment and truncation textures of CGM suggest Ta (and Nb) remobilization.

9. Concluding remarks

High-resolution chemical mapping of muscovite and columbite–tantalite allow reconstruction of complex crystallization processes. Melt–melt–fluid immiscibility during the magmatic–hydrothermal transition, which was previously proposed from experiments and fluid inclusion studies (Thomas et al., 2012; Thomas and Davidson, 2016), has been demonstrated by chemical mapping. The analytical approach allowed correlation not only of mineral zones between different grains, but also of two mineral species, resulting in our proposed three-stage model.

The importance of aqueous media and at what point aqueous and silicic media coexist during pegmatite formation is still debated in the literature (e.g. Černý et al., 2005; Thomas et al., 2012; London, 2014; Thomas and Davidson, 2015). However, the authors agree that H_2O-dominated phases become more important as complete pegmatite solidification is approached. The transition from purely magmatic stage I to the magmatic-metasomatic stage II must be achieved by a change of the crystallizing medium. Furthermore, oscillations in mineral composition and habit clearly show that at least two different media were involved after stage I.

Crystallization of columbite group minerals in Leinster rare-element pegmatites is both magmatic and hydrothermal. The increased abundance of CGM in replacive albitite units is likely caused by inheritance of early magmatic grains from resorbed magmatic units

and additional growth within the albitite-forming medium. Furthermore, Nb and Ta can be remobilized by digestion of CGM during the magmatic–hydrothermal transition. Similar processes were observed for example by Dewaele et al. (2011) in Rwanda.

The high-resolution chemical mapping approach used here allows deciphering of these complex rocks with small suite of samples. Analyzing two different mineral species, which co-crystallize and incorporate similar elements of interest, allows rigorous reconstruction of melt evolution. Columbite–tantalite and mica both incorporate HFSE and their crystallization is strongly influenced by network modifiers in the liquid. This makes combined analysis of CGM and mica a more suitable approach for understanding pegmatite-forming processes compared to studying Nb–Ta oxides alone. *In-situ* LA-ICP-MS chemical mapping of rock-forming minerals (muscovite) and associated accessory minerals (CGM) combined with geochemical modeling is therefore a powerful tool to reconstruct crystallization histories and to decipher the *mineralogical record* of igneous processes.

Muscovite zones of stage III constitute up to 25% of individual grains and differ significantly from the rest of the grains. As a result of reversed fractionation trends in stage III, bulk data for muscovite cannot be used as an accurate indicator for magmatic fractionation at the magmatic–hydrothermal transition. Furthermore, even point analyses might yield ‘mixed’ signals or might over-represent late stages, if they are not carefully placed or the spot ablation diameters are large. However, whole-grain or bulk data with a large range from high to low K/Rb might still be adequate for regional geochemical estimations.

Fractionation of Ta and Nb controlled by mica crystallization was demonstrated before for granitic melts by Stepanov et al. (2014). Our results show that crystallization of muscovite is also effective in changing Ta/Nb of pegmatite melts, but is furthermore controlled by the partitioning behavior of Nb and Ta in the presence of saline aqueous media. For mineral exploration for Ta and Cs, the discussed late stages are of highest interest. Both elements are remobilized, but do not necessarily precipitate again within the pegmatite body and may be lost to country rocks.

Based on the microtextural and geochemical observations presented here, we moreover propose that pegmatite albitization during stage III is accomplished by a hydrothermal fluid rather than a highly-fluxed melt. We suggest that albite precipitation is caused by a chemical quench, not by sudden loss of network modifiers from a silicate melt, but by change of Na^+ and K^+ activities and pH of the albite-forming saline hydrothermal fluid. The system appears to remain close to the albite–microcline–white-mica stability triple

point (Fig. 1 in Wibberley and McCaig, 2000), as all three phases are either precipitated, resorbed or both. After precipitation, the small grain size and microporosity of hydrothermal albite facilitate migration of the remaining fluid through the pegmatite body and into the host rock.

The proposed three-step process during magmatic–hydrothermal transition in the Leinster rare-element pegmatites from a system dominated (I) by a single silicic melt, (II) by two melts (silicic and aqueous) in conjunction with a hydrothermal fluid and (III) by hydrothermal processes, might also happen at the transition from fertile granite magma to formation of other granite-related orebodies (c.f. Černý et al., 2005) such as Mo-Sn-W-rich greisens and veins, and disseminated magmatic–hydrothermal mineralization (Cu, Au, rare-earth elements, HFSE).

Acknowledgements

We would like to thank John Harrop and the team of Blackstairs Lithium Ltd for access to drill cores and exploration data, and their assistance; Koen Torremans (iCRAG, University College Dublin [UCD]) for fruitful feedback about presenting the data and scientific discussions; Tom Culligan (UCD) for thin sectioning; and Daniel Kontak (Laurentian University) for stimulating discussions in the field. We further thank Rainer Thomas and two anonymous referees for their reviews and Edward M. Ripley for the editorial handling of the manuscript. This work was supported in part by Science Foundation Ireland [Grant Number 13/RC/2092] and is co-funded under the European Regional Development Fund and by iCRAG industry partners.

References

Anderson, M.O., Lentz, D.R., McFarlane, C.R.M. and Falck, H. (2013) A geological, geochemical and textural study of an LCT pegmatite: implications for the magmatic versus metasomatic origin of Nb-Ta mineralization in the Moose II pegmatite, Northwest Territories, Canada. Journal of Geosciences 58, 299–320.

Aseri, A.A., Linnen, R.L., Che, X.D., Thibault, Y. and Holtz, F. (2015) Effects of fluorine on the solubilities of Nb, Ta, Zr and Hf minerals in highly fluxed water-saturated haplogranitic melts. Ore Geology Reviews 64, 736–746.

Ayers, J.C. and Watson, E.B. (1991) Solubility of apatite, monazite, zircon, and rutile in supercritical aqueous fluids with implications for subduction zone geochemistry. Philosophical Transactions of the Royal Society of London. Series A: Physical and Engineering Sciences 335, 365–375.

1244 Badanina, E.V., Sitnikova, M.A., Gordiyenko, V.V., Melcher, F., Gäbler, H.E., Lodziak, J.
1245 and Syritso, L.F. (2015) Mineral chemistry of columbite–tantalite from spodumene
1246 pegmatites of Kolmozero, Kola Peninsula (Russia). Ore Geology Reviews 64, 720–735.
1247 Barros, R. (2017) Petrogenesis of the Leinster LCT (Li-Cs-Ta) pegmatite belt in southeast
1248 Ireland (PhD Thesis), School of Earth Sciences. University College Dublin, Dublin, p. 287.
1249 Barros, R. and Menuge, J.F. (2016) The origin of spodumene pegmatites associated with the
1250 Leinster Granite in southeast Ireland. The Canadian Mineralogist 54, 847–862.
1251 Bea, F., Pereira, M.D. and Stroh, A. (1994) Mineral/leucosome trace-element partitioning in a
1252 peraluminous migmatite (a laser ablation-ICP-MS study). Chemical Geology 117, 291–312.
1253 Černý, P., Blevin, P.L., Cuney, M. and London, D. (2005) Granite-related ore deposits.
1254 Economic Geology 100th Anniversary Volume, 337–370.
1255 Černý, P. and Burt, D.M. (1984) Paragenesis, crystallochemical characteristics, and
1256 geochemical evolution of micas in granite pegmatites, in: Bailey, S.W. (Ed.), Reviews in
1257 Mineralogy (13): Micas, pp. 257–297.
1258 Černý, P. and Ercit, T.S. (1985) Some recent advances in the mineralogy and geochemistry of
1259 Nb and Ta in rare-element granitic pegmatites. Bulletin de Minéralogie 108, 499–532.
1260 Černý, P. and Ercit, T.S. (2005) The classification of granitic pegmatites revisited. The
1261 Canadian Mineralogist 43, 2005–2026.
1262 Clarke, D.B. and Bogutyn, P.A. (2003) Oscillatory epitactic-growth zoning in biotite and
1263 muscovite from the Lake Lewis leucogranite, South Mountain Batholith, Nova Scotia,
1264 Canada. The Canadian Mineralogist 41, 1027–1047.
1265 Dewaele, S., Henjes-Kunst, F., Melcher, F., Sitnikova, M., Burgess, R., Gerdes, A.,
1266 Fernandez, M.A., Clercq, F.D., Muchez, P. and Lehmann, B. (2011) Late Neoproterozoic
1267 overprinting of the cassiterite and columbite-tantalite bearing pegmatites of the Gatumba
1268 area, Rwanda (Central Africa). Journal of African Earth Sciences 61, 10–26.
1269 Fenn, P.M. (1986) On the origin of graphic granite. American Mineralogist 71, 325–330.
1270 Fiege, A., Kirchner, C., Holtz, F., Linnen, R.L. and Dziony, W. (2011) Influence of fluorine
1271 on the solubility of manganotantalite ($MnTa_2O_6$) and manganocolumbite ($MnNb_2O_6$) in
1272 granitic melts – An experimental study. Lithos 122, 165–174.
1273 Fleet, M.E., Deer, W.A., Howie, R.A. and Zussman, J. (2003) Rock-Forming Minerals,
1274 Volume 3A: Mica, 2nd ed. The Geological Society, London.
1275 Foord, E.E. and Cook, R.B. (1989) Mineralogy and paragenesis of the McAllister Sn-Ta-
1276 bearing pegmatite, Coosa County, Alabama. The Canadian Mineralogist 27, 93–105.
1277 Ginibre, C., Wörner, G. and Kronz, A. (2007) Crystal zoning as an archive for magma
1278 evolution. Elements 3, 261–266.
1279 Gomes, M.E.P. and Neiva, A.M.R. (2000) Chemical zoning of muscovite from the Ervedosa
1280 granite, northern Portugal, Mineralogical Magazine, pp. 347–358.
1281 Gordiyenko, V.V. (1971) Concentrations of Li, Rb, and Cs in potash feldspar and muscovite
1282 as criteria for assessing the rare-metal mineralization in granite pegmatites. International
1283 Geology Review 13, 134–142.
1284 Hawthorne, F.C. and Černý, P. (1982) The mica group, in: Černý, P. (Ed.), Short Course in
1285 Granitic Pegmatites in Science and Industry. Mineralogical Association of Canada,
1286 Winnipeg, pp. 63–98.
1287 Holness, M.B. (2003) Growth and albitization of K-feldspar in crystalline rocks in the
1288 shallow crust: a tracer for fluid circulation during exhumation? Geofluids 3, 89–102.
1289 Hulsbosch, N., Boiron, M.-C., Dewaele, S. and Muchez, P. (2016) Fluid fractionation of
1290 tungsten during granite–pegmatite differentiation and the metal source of peribatholitic W
1291 quartz veins: Evidence from the Karagwe-Ankole Belt (Rwanda). Geochimica et
1292 Cosmochimica Acta 175, 299–318.

1293 Hulsbosch, N., Hertogen, J., Dewaele, S., André, L. and Muchez, P. (2014) Alkali metal and
1294 rare earth element evolution of rock-forming minerals from the Gatumba area pegmatites
1295 (Rwanda): Quantitative assessment of crystal-melt fractionation in the regional zonation of
1296 pegmatite groups. Geochimica et Cosmochimica Acta 132, 349–374.
1297 Icenhower, J. and London, D. (1995) An experimental study of element partitioning among
1298 biotite, muscovite, and coexisting peraluminous silicic melt at 200 MPa (H2O), American
1299 Mineralogist, pp. 1229–1251.
1300 Icenhower, J. and London, D. (1996) Experimental partitioning of Rb, Cs, Sr, and Ba
1301 between alkali feldspar and peraluminous melt, American Mineralogist, pp. 719–734.
1302 Jochum, K.P., Weis, U., Stoll, B., Kuzmin, D., Yang, Q., Raczek, I., Jacob, D.E., Stracke, A.,
1303 Birbaum, K., Frick, D.A., Günther, D. and Enzweiler, J. (2011) Determination of reference
1304 values for NIST SRM 610–617 glasses following ISO guidelines. Geostandards and
1305 Geoanalytical Research 35, 397–429.
1306 Jolliff, B.L., Papike, J.J. and Shearer, C.K. (1987) Fractionation trends in mica and
1307 tourmaline as indicators of pegmatite internal evolution: Bob Ingersoll pegmatite, Black
1308 Hills, South Dakota. Geochimica et Cosmochimica Acta 51, 519–534.
1309 Jolliff, B.L., Papike, J.J. and Shearer, C.K. (1992) Petrogenetic relationships between
1310 pegmatite and granite based on geochemistry of muscovite in pegmatite wall zones, Black
1311 Hills, South Dakota, USA. Geochimica et Cosmochimica Acta 56, 1915–1939.
1312 Keppler, H. (1993) Influence of fluorine on the enrichment of high field strength trace
1313 elements in granitic rocks. Contributions to Mineralogy and Petrology 114, 479–488.
1314 Kontak, D.J. (2006) Nature and origin of an LCT-suite pegmatite with late-stage sodium
1315 enrichment, Brazil Lake, Yarmouth County, Nova Scotia. I. Geological setting and petrology.
1316 The Canadian Mineralogist 44, 563–598.
1317 Lahti, S.I. (1987) Zoning in columbite–tantalite crystals from the granitic pegmatites of
1318 Eräjärvi area, southern Finland. Geochimica et Cosmochimica Acta 51, 509–517.
1319 Linnen, L.R. and Cuney, M. (2005) Granite-related rare-element deposits and experimental
1320 constrains oin Ta-Nb-W-Sb-Zr-Hf mineralization, in: Linnen, L.R., Samson, I.M. (Eds.),
1321 Rare-element geochemistry and mineral deposits. GAC Short Course Notes 17. Geological
1322 Association of Canada, St. Catharines, Ontario, pp. 48–68.
1323 Linnen, R.L. (1998) The solubility of Nb-Ta-Zr-Hf-W in granitic melts with Li and Li + F;
1324 constraints for mineralization in rare metal granites and pegmatites Economic Geology 93,
1325 1013–1025.
1326 Linnen, R.L., Trueman, D.L. and Burt, R. (2014) Tantalum and Niobium, in: Gunn, G. (Ed.),
1327 Critical Metals Handbook. John Wiley & Sons, Oxford, pp. 361–384.
1328 Linnen, R.L., Van Lichtervelde, M. and Černý, P. (2012) Granitic pegmatites as sources of
1329 strategic metals. Elements 8, 275–280.
1330 London, D. (2005) Geochemistry of alkali and alkaline earth elements in ore-forming
1331 granites, pegmatites, and rhyolites, in: Linnen, L.R., Samson, I.M. (Eds.), Rare-element
1332 geochemistry and mineral deposits. GAC Short Course Notes 17. Geological Association of
1333 Canada, St. Catharines, Ontario, pp. 17–44.
1334 London, D. (2014) A petrologic assessment of internal zonation in granitic pegmatites. Lithos
1335 184–187, 74–104.
1336 London, D., Morgan, G.B. and Icenhower, J. (1998) Stability and solubility of pollucite in the
1337 granite system at 200 MPa H2O. The Canadian Mineralogist 36, 497–510.
1338 Luecke, W. (1981) Lithium pegmatites in the Leinster Granite (Southeast Ireland). Chemical
1339 Geology 34, 195–233.
1340 Lumpkin, G.R. (1998) Rare-element mineralogy and internal evolution of the Rutherford# 2
1341 Pegmatite, Amelia County, Virginia; a classic locality revisited. The Canadian Mineralogist
1342 36, 339–353.

1343 Marchal, K.L., Simmons, W.B., Falster, A.U., Webber, K.L. and Roda-Robles, E. (2014)
1344 Geochemistry, Mineralogy and Evolution of Mica and Feldspar from the Mount Mica
1345 Pegmatite, Maine, USA. The Canadian Mineralogist 52, 221–233.
1346 McArdle, P. and Kennan, P.S. (1988) Controls on the Occurrence and Distribution of
1347 Tungsten and Lithium Deposits on the Southeast Margin of the Leinster Granite, Ireland, in:
1348 Boissonnas, J., Omenetto, P. (Eds.), Mineral Deposits within the European Community.
1349 Springer Berlin Heidelberg, Berlin, Heidelberg, pp. 199–209.
1350 McArdle, P. and Kennan, P.S. (1992) Deformational and stratigraphic influences on
1351 mineralization in SE Ireland. Mineralium Deposita 27, 213–218.
1352 McArdle, P. and Kennedy, M.J. (1985) The East Carlow Deformation Zone and its regional
1353 implications. Geological Survey of Ireland Bulletin 3, 237–255.
1354 Möller, P. and Morteani, G. (1987) Geochemical exploration guide for tantalum pegmatites.
1355 Economic Geology 82, 1888–1897.
1356 Morteani, G. and Gaupp, R. (1989) Geochemical Evaluation of the Tantalum Potential of
1357 Pegmatites, in: Möller, P., Černý, P., Saupé, F. (Eds.), Lanthanides, Tantalum and Niobium:
1358 Mineralogy, Geochemistry, Characteristics of Primary Ore Deposits, Prospecting, Processing
1359 and Applications Proceedings of a workshop in Berlin, November 1986. Springer Berlin
1360 Heidelberg, Berlin, Heidelberg, pp. 303–310.
1361 Mulja, T., Williams-Jones, A.E., Martin, R.F. and Wood, S.A. (1996) Compositional
1362 variation and structural state of columbite-tantalite in rare-element granitic pegmatites of the
1363 Preissac-Lacorne batholith, Quebec, Canada. American Mineralogist 81, 146–157.
1364 Murdaugh, A.E., Liddelow, M., Schmidt, A.M. and Manne, S. (2007) Two-Dimensional
1365 Crystal Growth from Undersaturated Solutions. Langmuir 23, 5852–5856.
1366 Nash, W.P. and Crecraft, H.R. (1985) Partition coefficients for trace elements in silicic
1367 magmas. Geochimica et Cosmochimica Acta 49, 2309–2322.
1368 Nassar, N.T. (2017) Shifts and trends in the global anthropogenic stocks and flows of
1369 tantalum. Resources, Conservation and Recycling 125, 233–250.
1370 Neiva, A.M.R. (2013) Micas, feldspars and columbite–tantalite minerals from the zoned
1371 granitic lepidolite-subtype pegmatite at Namivo, Alto Ligonha, Mozambique. European
1372 Journal of Mineralogy 25, 967–985.
1373 Norberg, N., Neusser, G., Wirth, R. and Harlov, D. (2011) Microstructural evolution during
1374 experimental albitization of K-rich alkali feldspar. Contributions to Mineralogy and
1375 Petrology 162, 531–546.
1376 Novák, M., Černý, P. and Uher, P. (2003) Extreme variation and apparent reversal of Nb-Ta
1377 fractionation in columbite-group minerals from the Scheibengraben beryl-columbite granitic
1378 pegmatite, Maršíkov, Czech Republic. European Journal of Mineralogy 15, 565–574.
1379 O'Connor, P.J., Gallagher, V. and Kennan, P.S. (1991) Genesis of lithium pegmatites from
1380 the leinster granite margin, Southeast Ireland: Geochemical constraints. Geological Journal
1381 26, 295–305.
1382 Parker, R.L. and Fleischer, M. (1968) Geochemistry of niobium and tantalum. US Geological
1383 Survrey Professional Paper 612, 1–43.
1384 Partington, G.A., McNaughton, N.J. and Williams, I.S. (1995) A review of the geology,
1385 mineralization, and geochronology of the Greenbushes Pegmatite, Western Australia.
1386 Economic Geology 90, 616–635.
1387 Paton, C., Hellstrom, J., Paul, B., Woodhead, J.D. and Hergt, J.M. (2011) Iolite: Freeware for
1388 the visualisation and processing of mass spectrometric data. Journal of Analytical Atomic
1389 Spectrometry 26, 2508–2518.
1390 Pesquera, A., Torres Ruiz, J., Gil Crespo, P.P. and Velilla, N. (1999) Chemistry and genetic
1391 implications of tourmaline and Li-F-Cs micas from the Valdeflores area (Caceres, Spain).
1392 American Mineralogist 84, 55–69.

1393 Petrus, J.A., Chew, D.M., Leybourne, M.I. and Kamber, B.S. (2017) A new approach to
1394 laser-ablation inductively-coupled-plasma mass-spectrometry (LA-ICP-MS) using the
1395 flexible map interrogation tool 'Monocle'. Chemical Geology 463, 76–93.
1396 Philpotts, J.A. and Schnetzler, C.C. (1970) Phenocryst-matrix partition coefficients for K, Rb,
1397 Sr and Ba, with applications to anorthosite and basalt genesis. Geochimica et Cosmochimica
1398 Acta 34, 307–322.
1399 Plümper, O. and Putnis, A. (2009) The complex hydrothermal history of granitic rocks:
1400 Multiple feldspar replacement reactions under subsolidus conditions. Journal of Petrology 50,
1401 967–987.
1402 Putnis, A. and Austrheim, H. (2010) Fluid-induced processes: metasomatism and
1403 metamorphism. Geofluids 10, 254–269.
1404 Raimbault, L. and Burnol, L. (1998) The Richemont rhyolite dyke, Massif Central, France; a
1405 subvolcanic equivalent of rare-metal granites. The Canadian Mineralogist 36, 265–282.
1406 Rickers, K., Thomas, R. and Heinrich, W. (2006) The behavior of trace elements during the
1407 chemical evolution of the H2O-, B-, and F-rich granite–pegmatite–hydrothermal system at
1408 Ehrenfriedersdorf, Germany: a SXRF study of melt and fluid inclusions. Mineralium
1409 Deposita 41, 229–245.
1410 Roda-Robles, E., Keller, P., Pesquera, A. and Fontan, F. (2007) Micas of the muscovite–
1411 lepidolite series from Karibib pegmatites, Namibia. Mineralogical Magazine 71, 41–62.
1412 Roda-Robles, E., Pesquera, A., Gil-Crespo, P. and Torres-Ruiz, J. (2012) From granite to
1413 highly evolved pegmatite: A case study of the Pinilla de Fermoselle granite–pegmatite system
1414 (Zamora, Spain). Lithos 153, 192–207.
1415 Roda-Robles, E., Pesquera Peréz, A. and Velasco Roldán, F. (1995) Micas of the muscovite-
1416 lepidolite series from the fregeneda pegmatites (Salamanca, Spain). Mineralogy and
1417 Petrology 55, 145–157.
1418 Romer, R.L. and Wright, J.E. (1992) U-Pb dating of columbites: A geochronologic tool to
1419 date magmatism and ore deposits. Geochimica et Cosmochimica Acta 56, 2137–2142.
1420 Roycroft, P. (1991) Magmatically zoned muscovite from the peraluminous two-mica granites
1421 of the Leinster batholith, southeast Ireland. Geology 19, 437–440.
1422 Selway, J.B., Breaks, F.W. and Tingle., A.G. (2005) A Review of Rare-Element (Li-Cs-Ta)
1423 Pegmatite Exploration Techniques for the Superior Province, Canada, and Large Worldwide
1424 Tantalum Deposits. Exploration and Mining Geology 14, 1–30.
1425 Siegel, K., Wagner, T., Trumbull, R.B., Jonsson, E., Matalin, G., Wälle, M. and Heinrich,
1426 C.A. (2016) Stable isotope (B, H, O) and mineral-chemistry constraints on the magmatic to
1427 hydrothermal evolution of the Varuträsk rare-element pegmatite (Northern Sweden).
1428 Chemical Geology 421, 1–16.
1429 Smith, E.F. (1905) Observations on Columbium and Tantalum. Proceedings of the American
1430 Philosophical Society 44, 151–158.
1431 Sowerby, J.R. and Keppler, H. (2002) The effect of fluorine, boron and excess sodium on the
1432 critical curve in the albite–H2O system. Contributions to Mineralogy and Petrology 143, 32-
1433 37.
1434 Steiger, R. and von Knorring, O. (1974) A lithium pegmatite belt in Ireland. Journal of Earth
1435 Sciences, Leeds Geological Association 8, 433–443.
1436 Stepanov, A., A. Mavrogenes, J., Meffre, S. and Davidson, P. (2014) The key role of mica
1437 during igneous concentration of tantalum. Contributions to Mineralogy and Petrology 167,
1438 1009–1017.
1439 Sweetapple, M.T. and Collins, P.L.F. (2002) Genetic Framework for the Classification and
1440 Distribution of Archean Rare Metal Pegmatites in the North Pilbara Craton, Western
1441 Australia. Economic Geology 97, 873–895.

1442 Sylvester, P.J. and Jackson, S.E. (2016) A Brief History of Laser Ablation Inductively
1443 Coupled Plasma Mass Spectrometry (LA–ICP–MS). Elements 12, 307–310.
1444 Thomas, R. and Davidson, P. (2013) The missing link between granites and granitic
1445 pegmatites. Journal of Geosciences, 183–200.
1446 Thomas, R. and Davidson, P. (2015) Comment on "A petrologic assessment of internal
1447 zonation in granitic pegmatites" by David London (2014). Lithos 212-215, 462–468.
1448 Thomas, R. and Davidson, P. (2016) Revisiting complete miscibility between silicate melts
1449 and hydrous fluids, and the extreme enrichment of some elements in the supercritical state —
1450 Consequences for the formation of pegmatites and ore deposits. Ore Geology Reviews 72,
1451 1088–1101.
1452 Thomas, R., Davidson, P. and Beurlen, H. (2012) The competing models for the origin and
1453 internal evolution of granitic pegmatites in the light of melt and fluid inclusion research.
1454 Mineralogy and Petrology 106, 55–73.
1455 Thomas, R., Förster, H.-J. and Heinrich, W. (2003) The behaviour of boron in a peraluminous
1456 granite-pegmatite system and associated hydrothermal solutions: a melt and fluid-inclusion
1457 study. Contributions to Mineralogy and Petrology 144, 457–472.
1458 Tindle, A.G. and Breaks, F.W. (2000) Columbite-tantalite mineral chemistry from rare-
1459 element granitic pegmatites: Separation Lakeh area, N.W. Ontario, Canada. Mineralogy and
1460 Petrology 70, 165–198.
1461 Tischendorf, G., Gottesmann, B., Förster, H.-J. and Trumbull, R.B. (1997) On Li-bearing
1462 micas; estimating Li from electron microprobe analyses and an improved diagram for
1463 graphical representation. Mineralogical Magazine 61, 809–834.
1464 Ubide, T., McKenna, C.A., Chew, D.M. and Kamber, B.S. (2015) High-resolution LA-ICP-
1465 MS trace element mapping of igneous minerals: In search of magma histories. Chemical
1466 Geology 409, 157–168.
1467 Van Lichtervelde, M., Grégoire, M., Linnen, R.L., Béziat, D. and Salvi, S. (2008) Trace
1468 element geochemistry by laser ablation ICP-MS of micas associated with Ta mineralization
1469 in the Tanco pegmatite, Manitoba, Canada. Contributions to Mineralogy and Petrology 155,
1470 791–806.
1471 Van Lichtervelde, M., Linnen, R.L., Salvi, S. and Béziat, D. (2006) The role of metagabbro
1472 rafts on tantalum mineralization in the Tanco granitic pegmatite, Manitoba. The Canadian
1473 Mineralogist 44, 625–644.
1474 Van Lichtervelde, M., Melcher, F. and Wirth, R. (2009) Magmatic vs. hydrothermal origins
1475 for zircon associated with tantalum mineralization in the Tanco pegmatite, Manitoba, Canada.
1476 American Mineralogist 94, 439–450.
1477 Veksler, I.V. (2005) Element-enrichment and fractionation by magmatic aqueous fluids:
1478 experimental constraints on melt–fluid immiscibility and element partitioning, in: Linnen,
1479 L.R., Samson, I.M. (Eds.), Rare-element geochemistry and mineral deposits. GAC Short
1480 Course Notes 17. Geological Association of Canada, St. Catharines, Ontario, pp. 69–85.
1481 Viana, R.R., Evangelista, H.J. and Stern, W.B. (2007) Chemical zoning of muscovite
1482 megacrystal from the Brazilian Pegmatite Province. Anais da Academia Brasileira de
1483 Ciências 79, 431–439.
1484 Walker, R.J., Hanson, G.N. and Papike, J.J. (1989) Trace element constraints on pegmatite
1485 genesis: Tin Mountain pegmatite, Black Hills, South Dakota. Contributions to Mineralogy
1486 and Petrology 101, 290–300.
1487 Webster, J.D., Holloway, J.R. and Hervig, R.L. (1989) Partitioning of lithophile trace
1488 elements between H 2 O and H2O + CO2 fluids and topaz rhyolite melt. Economic Geology
1489 84, 116–134.
1490 Wibberley, C.A.J. and McCaig, A.M. (2000) Quantifying orthoclase and albite
1491 muscovitisation sequences in fault zones. Chemical Geology 165, 181–196.

Wise, M.A. (1995) Trace element chemistry of lithium-rich micas from rare-element granitic pegmatites. Mineralogy and Petrology 55, 203–215.
Wise, M.A. and Brown, C.D. (2011) Chemical composition of coexisting columbite-group minerals and cassiterite from the Black Mountain pegmatite, Maine. European Journal of Mineralogy 23, 817–828.
Wise, M.A., Francis, C.A. and Černý, P. (2012) Compositional and structural variations in columbite-group minerals from granitic pegmatites of the Brunswick and Oxford fields, Maine: Differential trends in F-poor and F-rich environments. The Canadian Mineralogist 50, 1515–1530.

1503

1504 **Figures and Tables**

1505

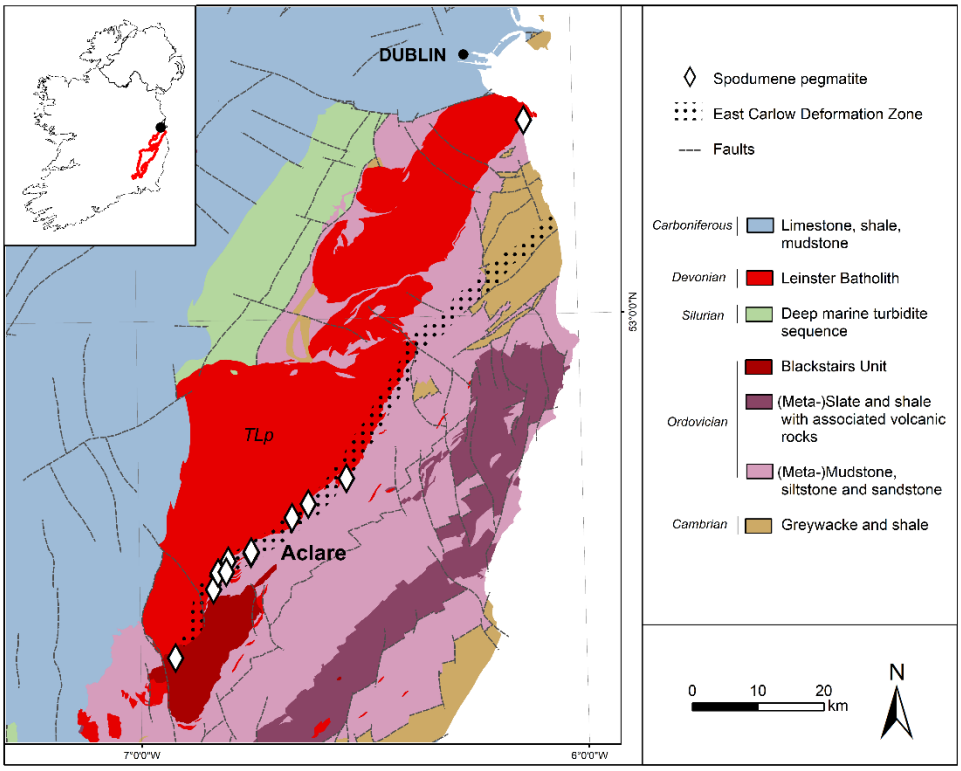

Fig. 1: Geological map of southeast Ireland. Spodumene pegmatite dikes (diamonds) are emplaced on the eastern margin of the Tullow Lowlands pluton (TLp) of the Leinster Batholith within the East Carlow Deformation Zone (McArdle and Kennedy, 1985). Map compiled with data from Geological Survey Ireland.

1506

1507

1508

1509

1510

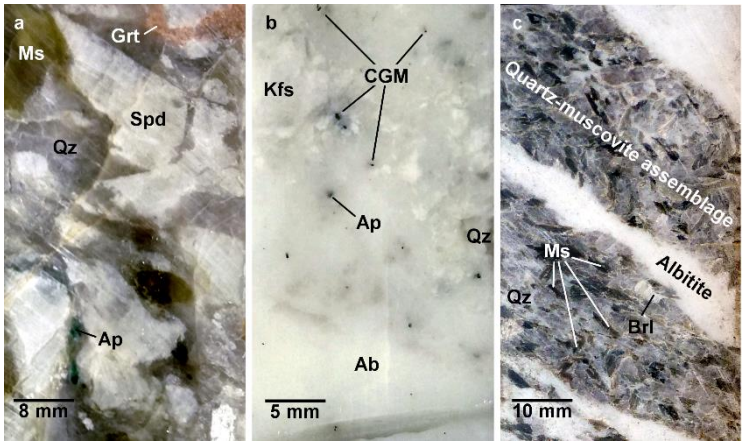

Fig. 2: Photographs of the different lithologies observed in drill core. **a:** Coarse-grained spodumene (Spd) pegmatite with abundant quartz (Qz) and muscovite (Ms), accessory garnet (Grt) and dark-green apatite (Ap). **b:** Albitite dominated by fine-grained granular albite (Ab) which is replacing coarse microcline (Kfs). Columbite–tantalite (CGM) is locally abundant. **c:** Bands of coarse-grained quartz-muscovite assemblage are common throughout the drill core. They are commonly intersected by albitite and bear beryl (Brl) and garnet.

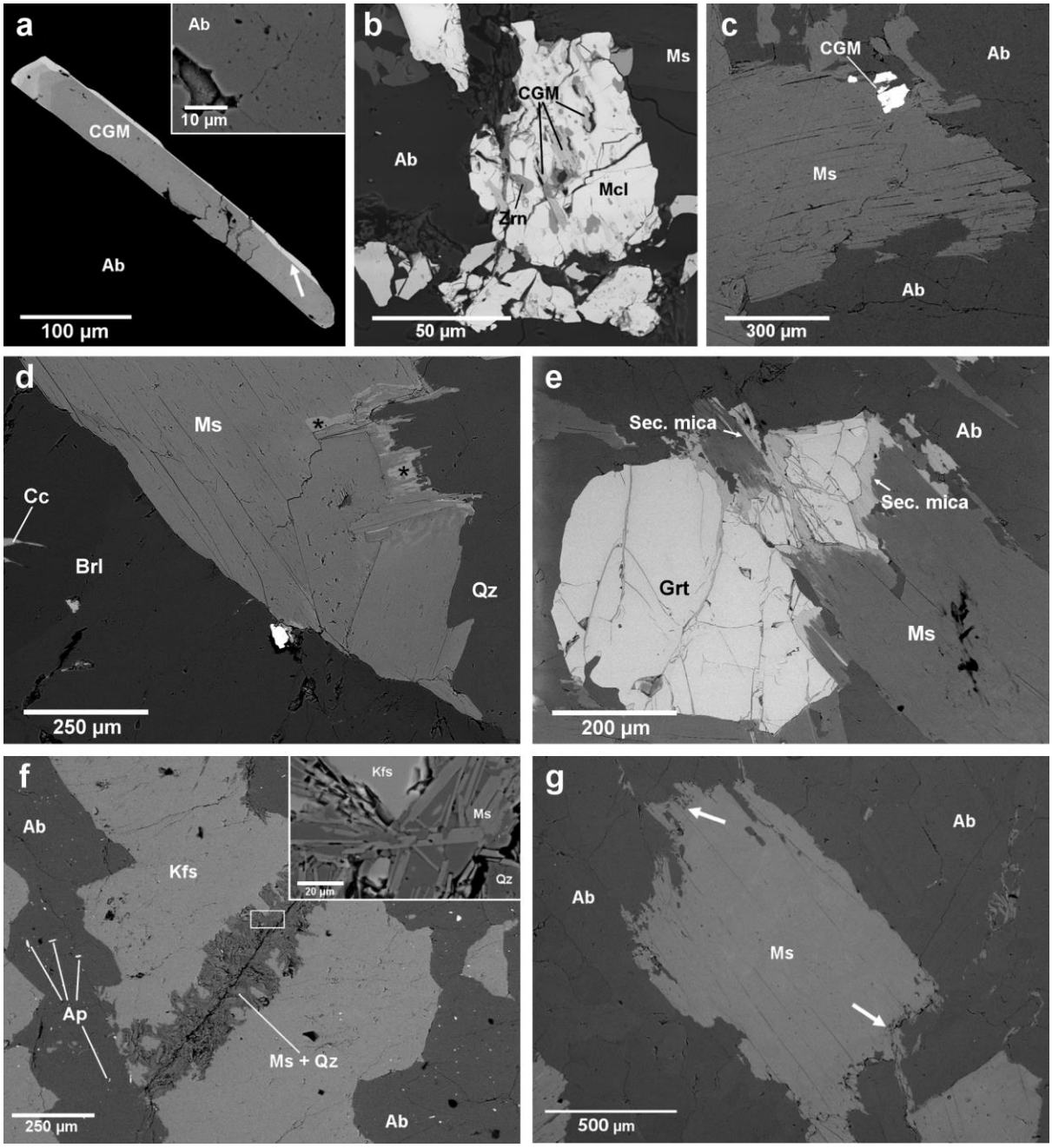

Fig. 3: Backscattered electron images of minerals in samples UB-A (a–c), QM-A (d–e) and LB-A (f–g). **a:** Elongate-prismatic columbite group mineral (CGM) with oscillatory zoning and Ta-rich overgrowth (arrow) between albite (Ab) laths. Inset: Microporosity in albite. **b:** Microlite (Mcl) overgrowing resorbed CGM and zircon (Zrn). **c:** Irregularly-shaped CGM associated with pegmatitic muscovite (Ms) in contact with albitite. **d:** Muscovite and quartz (Qz) in contact with beryl (Brl). The primary Ms flakes are partly replaced and overgrown by BSE-bright mica indicated by an asterisk (*). Beryl is partly replaced by calcite (Cc). **e:** Spessartine garnet (Grt) and muscovite partly replaced and overgrown by BSE-bright mica. **f:** Remnant microcline (Kfs) replaced by lath-shaped albite with minute subhedral apatite inclusions (Ap). Microcline is commonly fractured and replaced by fine-grained rose-colored mica and quartz (inset). **g:** Coarse muscovite in albite matrix overgrown by fine-grained mica (arrows).

1514

1515

1516

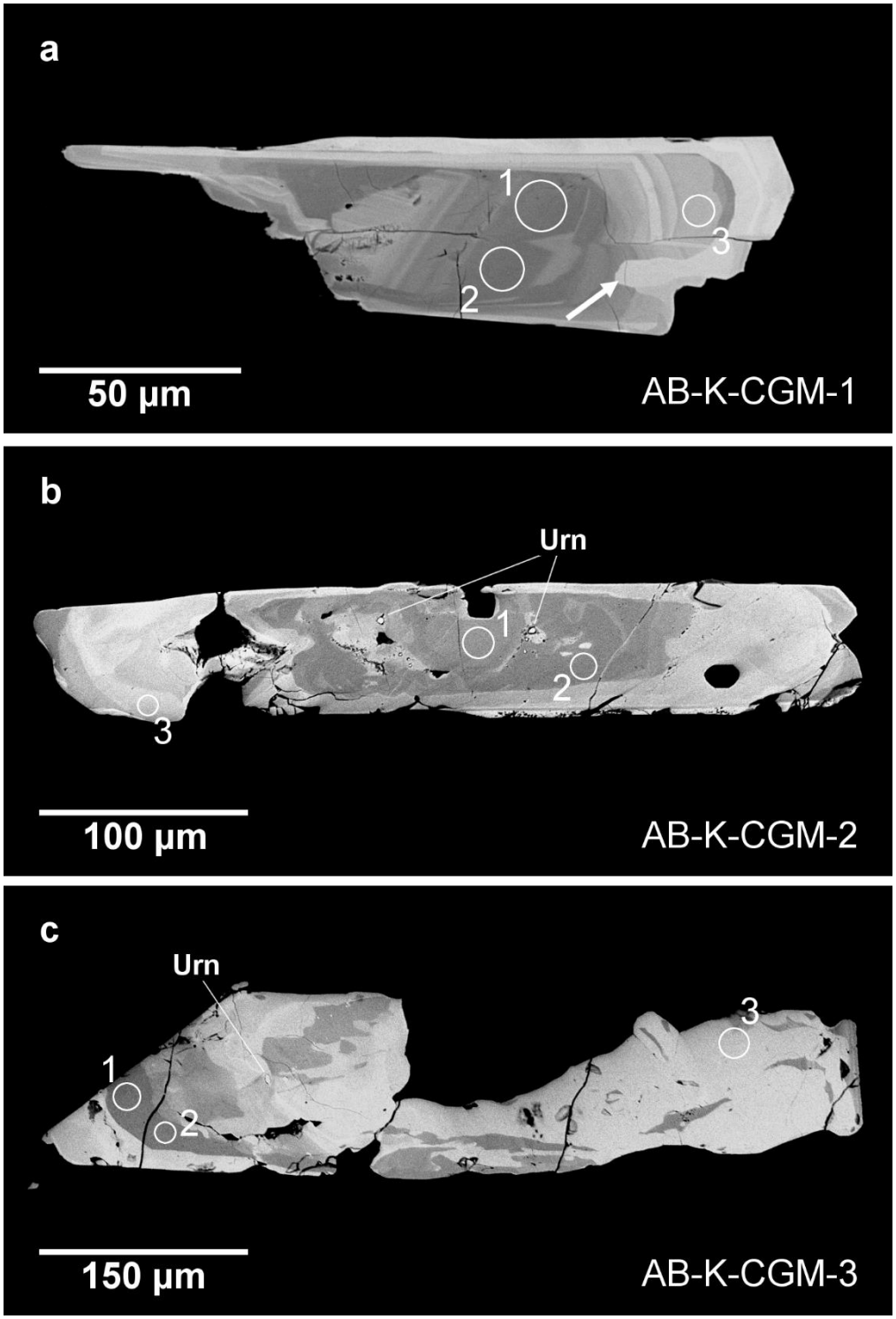

Fig. 4: Backscattered electron images of columbite group minerals (CGM) with uraninite (Urn) inclusions in sample LB-A. Major element analysis were analysed in the circled areas. **a:** Subhedral lath-shaped CGM with prominent oscillatory zoning within albitite. It shows signs of partial digestion and later overgrowth by Ta-enriched material (arrow). **b:** Anhedral elongate-prismatic CGM within albitite, close to former pegmatite. The zoning is less distinct and patchy in some areas. **c:** Subhedral to irregular elongate-prismatic CGM associated with pegmatitic muscovite and microcline. Zoning is patchy and irregular shape and truncation suggest partial digestion.

1517

1518

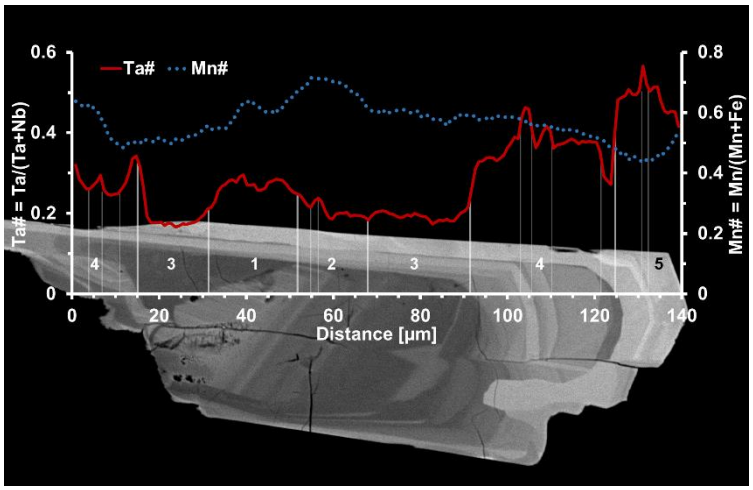

Fig. 5: SEM-EDS line-scan over LB-A-CGM-1 (Fig. 4a). Oscillatory zoning is mainly observed for strongly variable Ta# (solid red line) with overall increasing Ta# from core to rim. Mn# (dotted blue line) shows less variability: It decreases from core to rim initially, but increases in the Ta-enriched rims. The zones 1–5 refer to the zones defined based on the LA-ICP-MS images of this grain.

1519

1520

1521

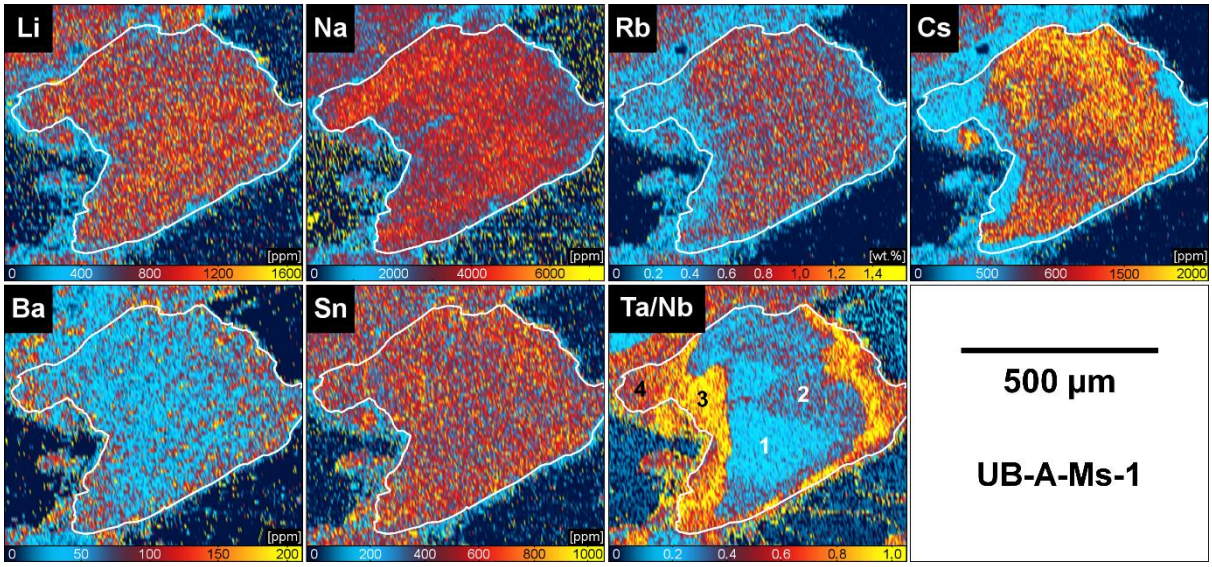

Fig. 6: LA-ICP-MS minor and trace element images of muscovite Ms-1 in albitite (sample UB-A). Four distinct growth zones were identified (numbers). The white line indicates the grain boundary as observed in reflected light.

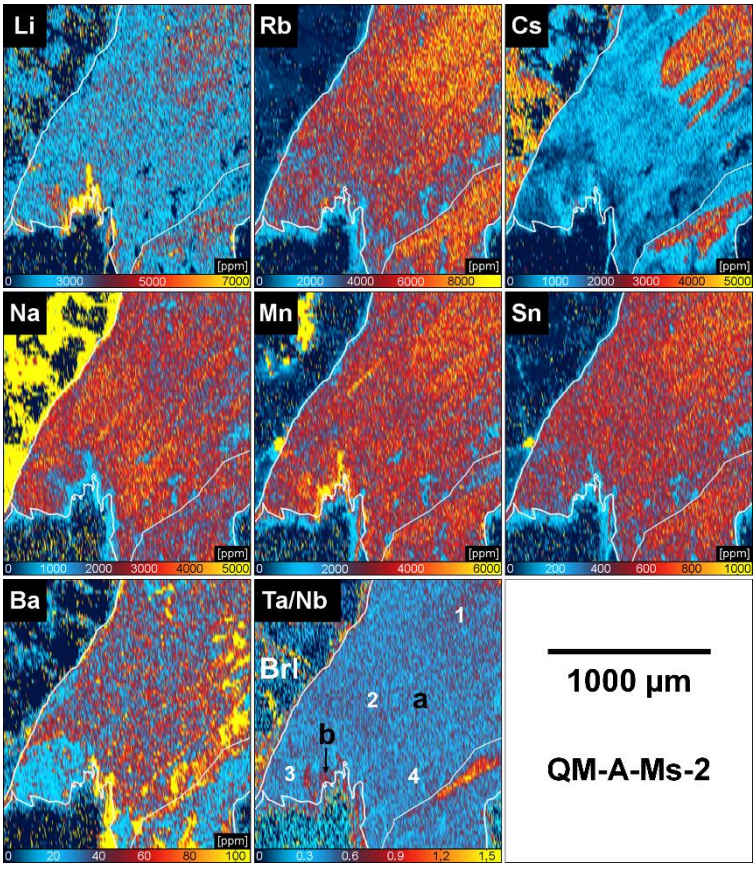

Fig. 7: LA-ICP-MS minor and trace element images of muscovite Ms-2 of the quartz–muscovite assemblage (sample QM-A). The mica is in contact with beryl (Brl) which is partly replaced by calcite. Four distinct growth zones were identified (numbers). The primary mica (a) is partly replaced by secondary mica (b). The white line indicates the grain boundary of muscovite as observed in reflected light.

1522

1523

1524

1525

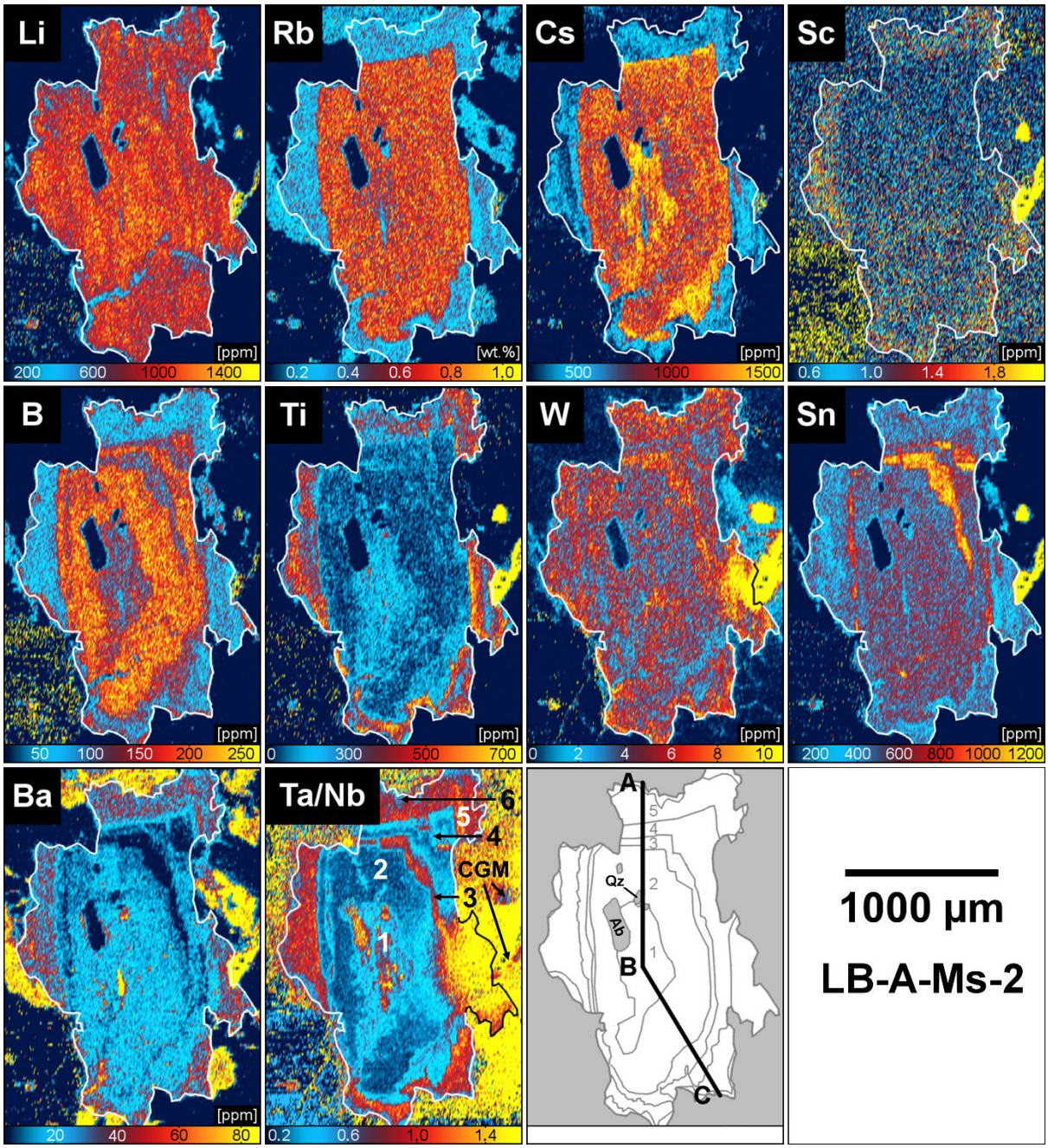

Fig. 8: LA-ICP-MS minor and trace element images of muscovite LB-A-Ms-2. The mica is in contact with microcline (high Ba), albite, and columbite (CGM). Six distinct growth zones were identified (numbers). The grain shows oscillatory zoning for most elements (B, Ba, Ti, Nb, Sn, Ta, W) and progressive zoning in Rb and Cs. This is followed by partial digestion and B-, Rb, and Cs-poor overgrowths (zones 5). The outline indicates the grain boundary as observed in reflected light. The last tile displays the location of the concentration profile, which is shown in Fig. 11.

1526

1527

1528

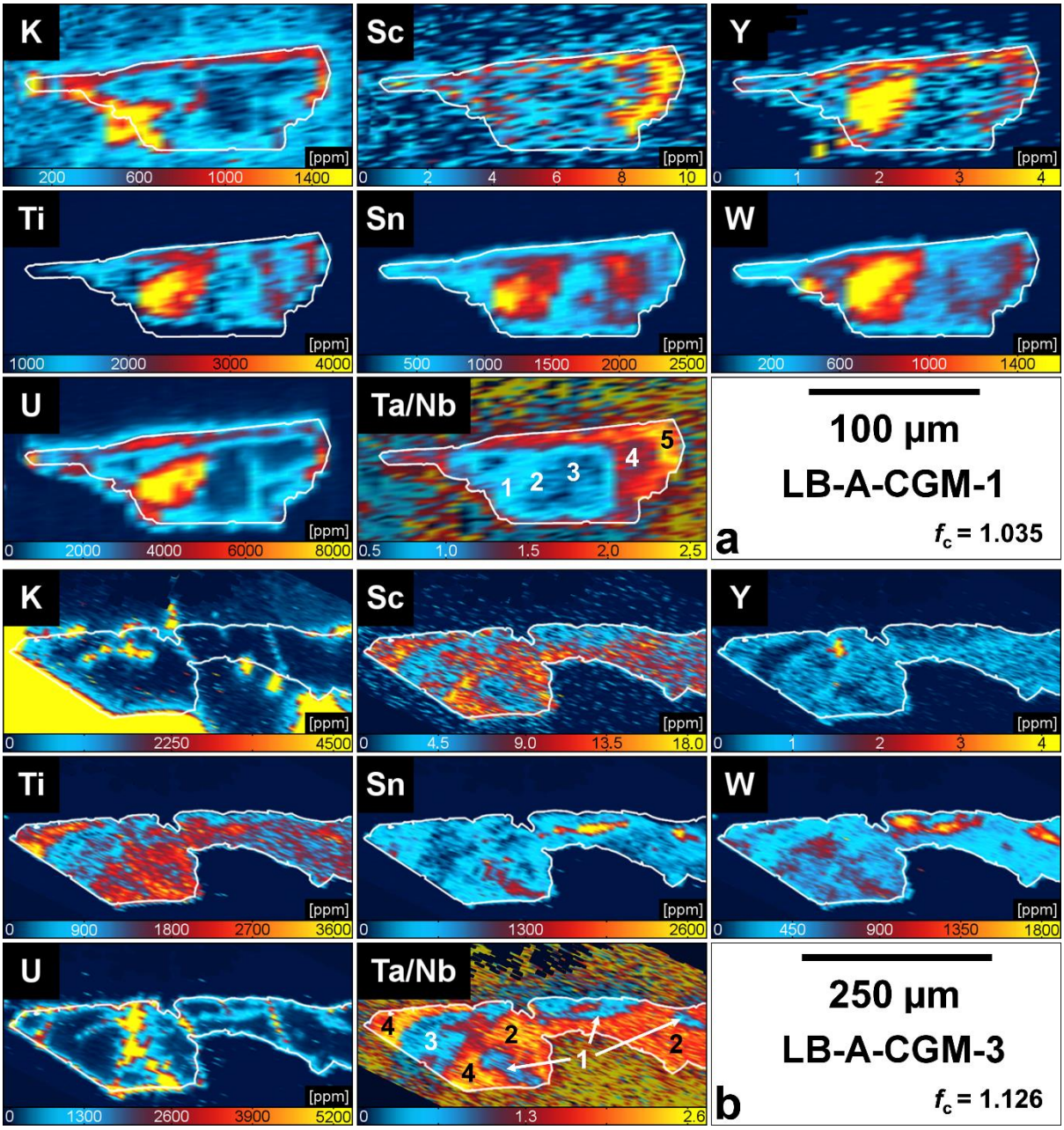

Fig. 9: Semi-quantitative LA-ICP-MS minor and trace elements images for columbite group minerals **a:** LB-A-CGM-1 within albitic portion of sample LB-A. From zone 1 to 3 in shows reverse zoning with decreasing Ta/Nb while the Ta-rich subhedral overgrowth (zones 4 and 5) shows normal zoning (increasing Ta/Nb). **b:** LB-A-CGM-3 is surrounded by albite and within the albitic portion of sample LB-A, but in contact to pegmatitic muscovite (high K). Only the boundary to muscovite is straight while the rest of the grain is strongly truncated. Four growth zones (numbers) were defined from the central parts to the upper left rim of the grain. The correction factors f_c (=$[Ta]_{Iolite}/[Ta]_{SEM-EDS}$) were used to correct the LA-ICP-MS data which was reduced without internal standard in a semi-quantitative mode of Iolite. Scales shown are corrected multiplication with f_c^{-1}.

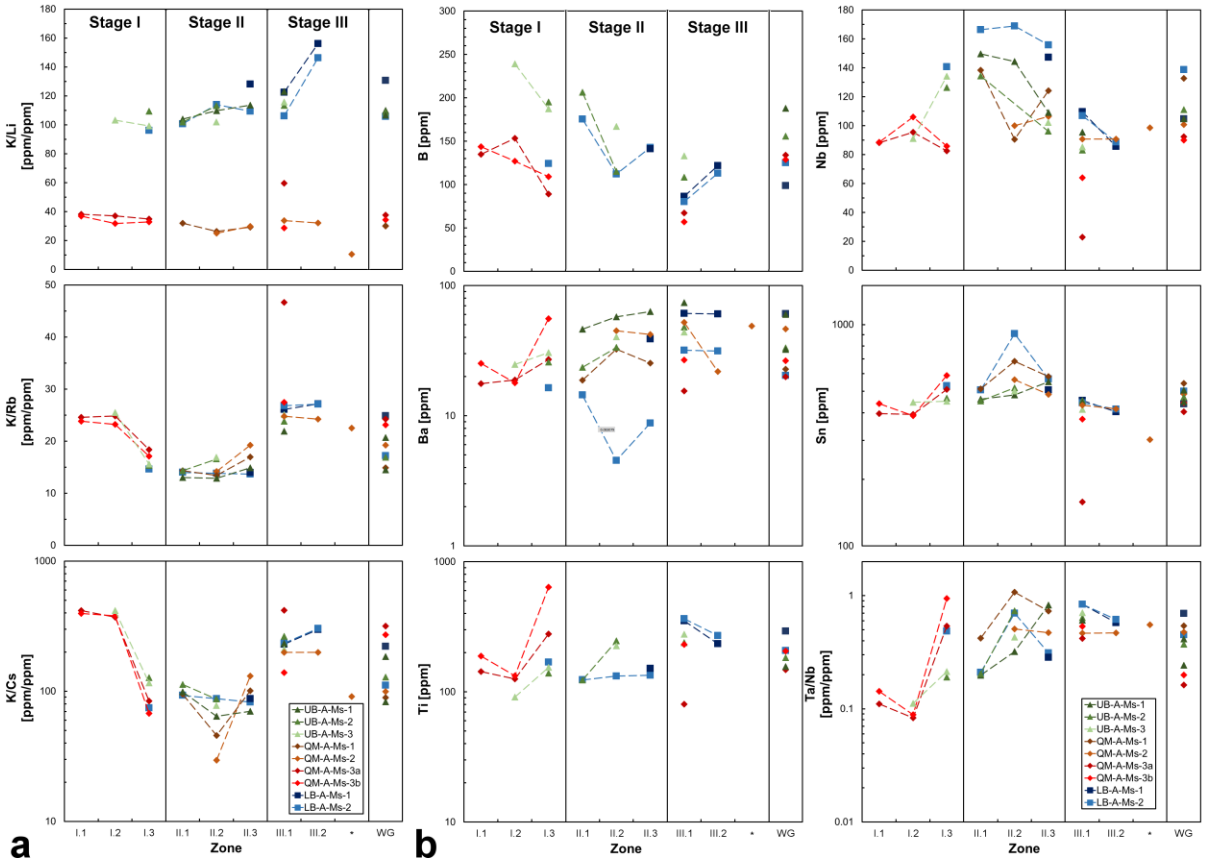

Fig. 10: Chemical variation in paragenetic stages and zones of all muscovite grains analyzed by LA-ICP-MS. Zones were correlated on basis of their K/Rb, K/Cs and K/Li patterns as shown in (**a**).Distribution of B, Ba and the high field strength elements Ti, Nb, Sn and Ta (expressed as Ta/Nb) in correlated mica growth zones is shown in (**b**). Samples from the upper border aplite (UB-A) are displayed in green (triangles), samples from the quartz muscovite assemblage are displayed in red (diamonds) and samples from the lower border aplite (LB-A) are displayed in blue (squares). Errors (2SE) for each element in the individual zones are generally <6% with most in the range of 1–3% (depending on the pixel area of individual zones). Absolute error values can be found in supplementary Table ST1.Three growth stages (I–III) were defined, based on resorption surfaces and trace element variations. Whole grain data (WG) is shown in the last column. The asterisk (*) on the x-axis marks replacive BSE-bright mica in sample QM-A.

1535

1536

1537

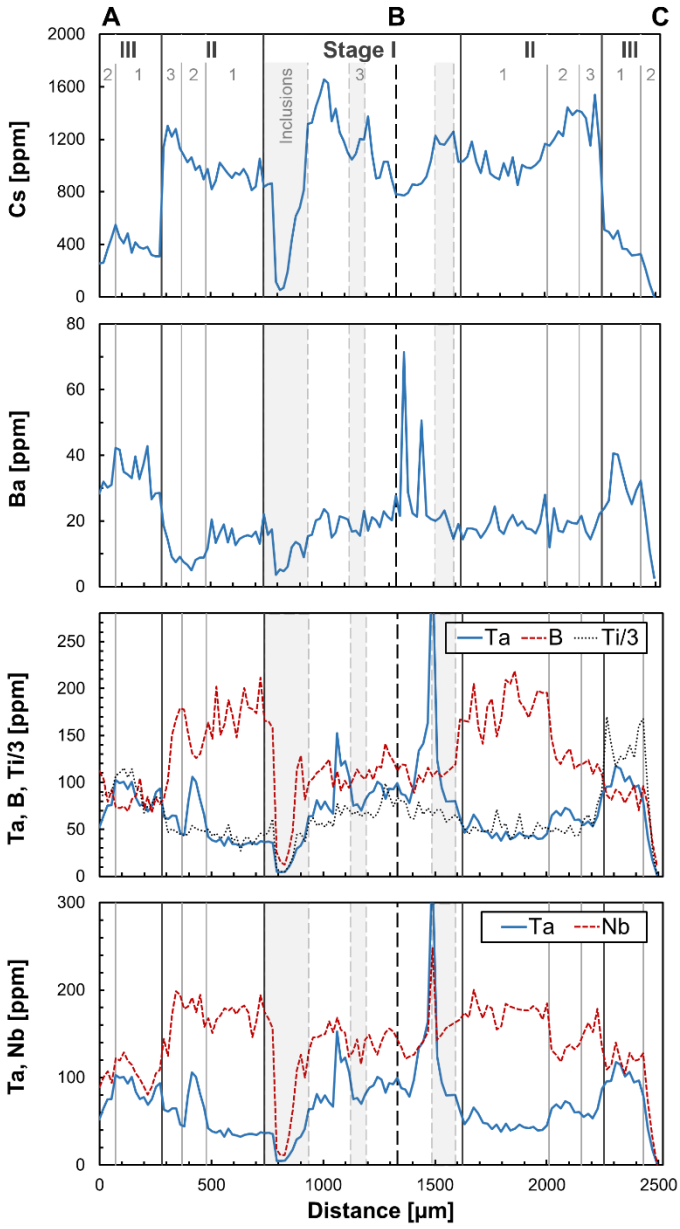

Fig. 11: Concentration profiles for Cs, Ba, B, Ti, Nb and Ta in muscovite LB-A-Ms-2 along the path shown in Fig. 10. Grey numbers refer to the individual zones of the crystal. Shaded areas mark inclusions. Stages I-III are the same as shown in Figs. 15 and 16. Cesium shows trends which would be expected for fractional crystallization of an incompatible element. Barium is depleted in stages I and II but enriched in stage III. Boron and Ta show anti-correlation, especially in the outer zones, while Ti and Ta seem correlated. Niobium and tantalum show clear anti-correlation for some zones, but correlation in others.

1538

1539

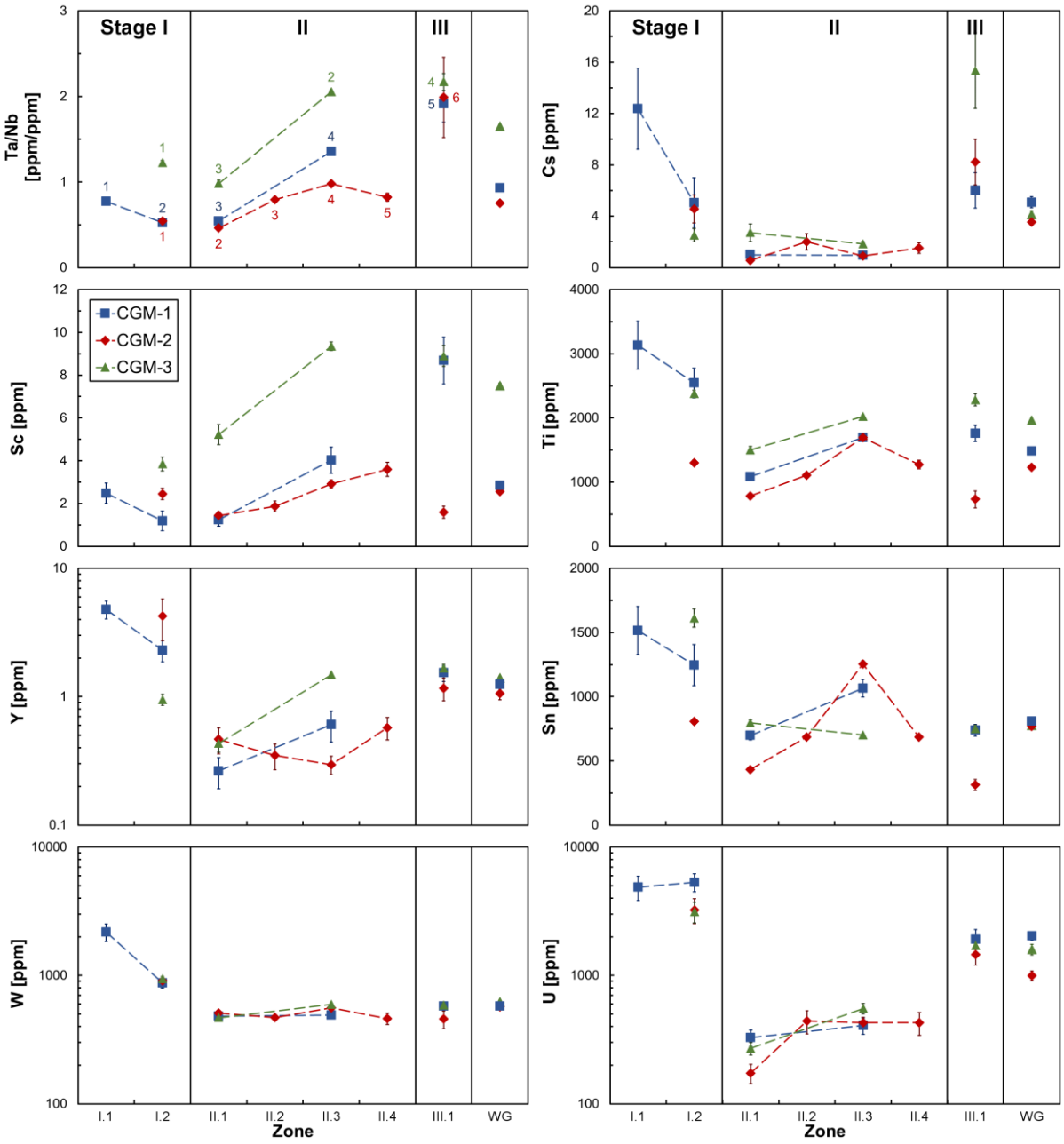

Fig 12: Correlated zones of columbite group minerals CGM-1 (squares), -2 (diamonds) and -3 (triangles) in the lower border aplite (sample LB-A) analyzed with LA-ICP-MS. Zones were correlated based on patterns of Ta/Nb, Ti, Y, Sn, W and U. The patterns can be subdivided into three stages (I–III) which are analogues to the stages observed in muscovite (Fig. 15).The error bars represent individual standard errors (2SE) for each zone (or whole grain) as exported from Iolite as well as propagated errors for Ta/Nb. WG: Whole grain.

1540

1541

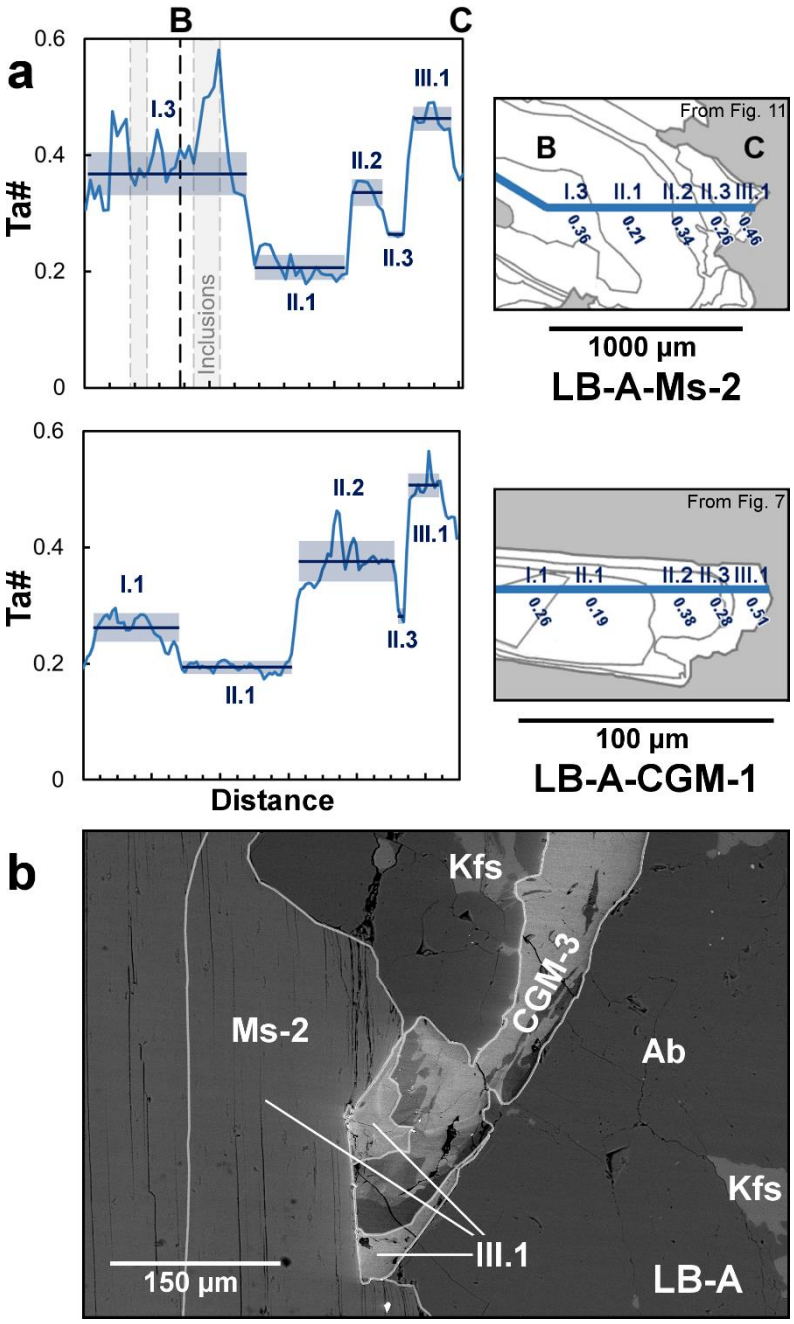

Fig. 13: Evidence for contemporaneous crystallization of columbite group minerals and white mica. **a:** Shown are profiles for Ta# = Ta/(Ta+Nb) in muscovite LB-A-Ms-2 (Fig. 11) and columbite group mineral LB-A-CGM-1. Roman numerals (I–III) indicate the stages of pegmatite formation. Solid bars and shaded areas on the plots (left) show the average Ta# for each zone and the respective standard deviations. Absolute values for average Ta# are shown on the sketches (right). The patterns are the same in both types of minerals, suggesting contemporaneous crystallization**. b:** Composite BSE image of LB-A-CGM-1 in contact to LB-A-Ms-2, which illustrates the temporal association of zones III.1 of both muscovite and CGM.

1542

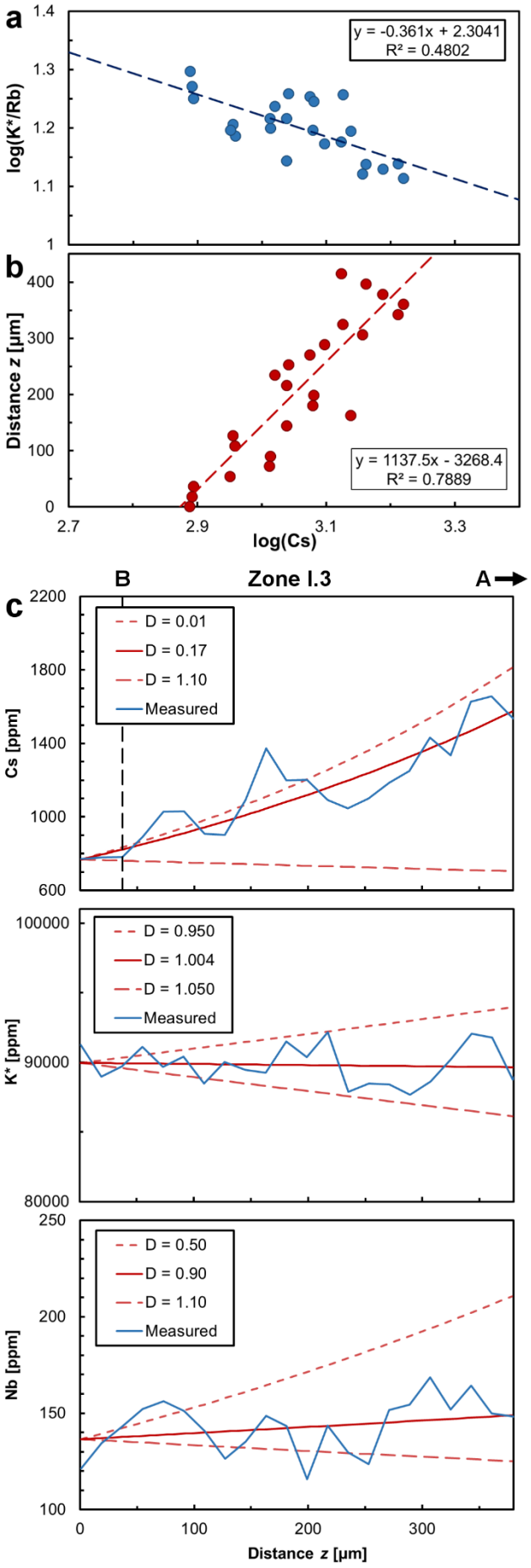

Fig. 14: Geochemical modeling of zone III.1 of muscovite LB-A-Ms-2. **a**: Slope and intercept of the linear relationship of log(K/Rb) vs log(Cs) depend on the bulk partition coefficients for each element as well as the starting composition of the crystallizing liquid. **b:** The distance *z* along the profile and log(Cs) show a linear relationship. This allows the melt fraction *F* to be inferred from the distance *z*. **c:** Modeled concentration for the concentration profiles of Cs, K and Nb in zone I.3 of muscovite LB-A-Ms-2 along the profile shown in Fig. 11 in direction B–A. Modeled concentrations are shown for different bulk partition coefficients D (red lines). Solid red lines represent D values which best fit the observed trends

1543

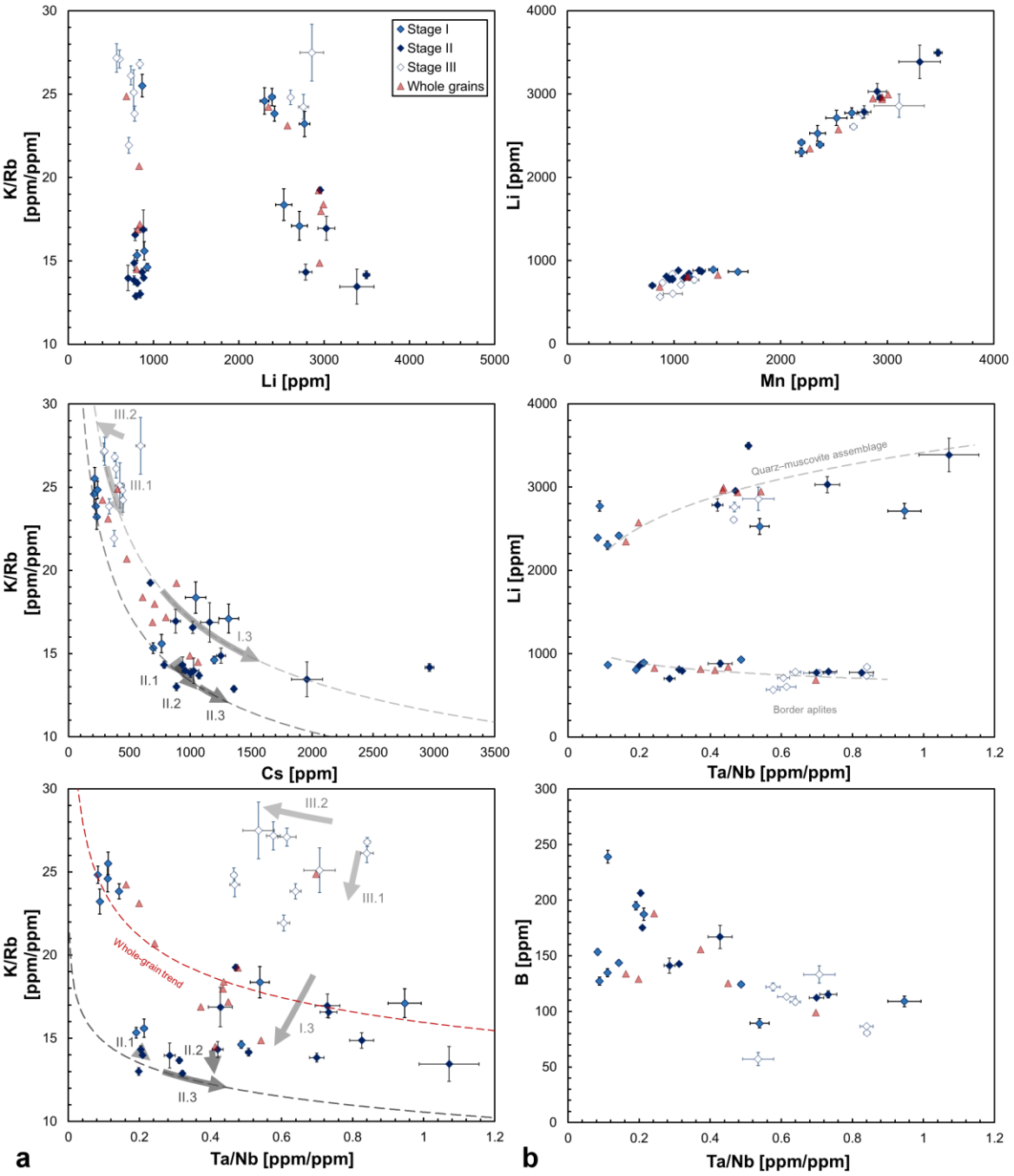

Fig. 15: Fractionation plots for rare elements in individual zones (diamonds) and whole grains (triangles) for all muscovite grains analyzed by LA-ICP-MS chemical mapping. The error bars represent individual standard errors (2SE) fear each zone (or whole grain) as exported from Iolite as well as propagated errors for element ratios. **a:** K/Rb v. Li, Cs and Ta#. Arrows in the K/Rb v. Cs and K/Rb v. Ta/Nb plots are the modelled concentration ranges for the concentration profiles across the six individual zone (I.3–III.2) of muscovite LB-A-Ms-2. **b**: Li v. Mn, Li v. Ta/Nb and B v. Ta/Nb. Trends for Li v. Ta from regression for power-law behavior.

1544

1545

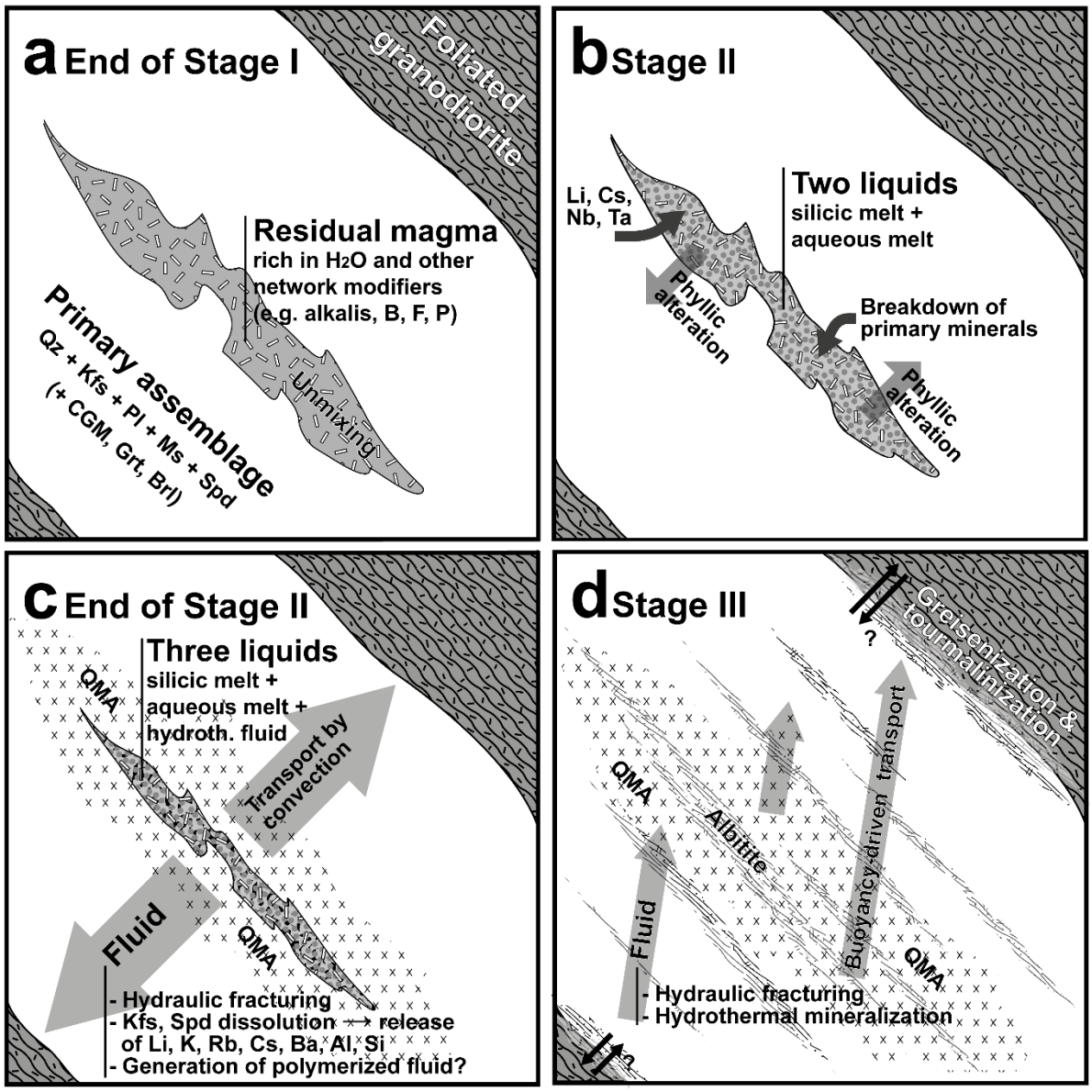

Fig. 16: Schematic illustration of our three-stage model of pegmatite crystallization summarizing the processes during magmatic–hydrothermal transition. **a:** Stage I marks the end of purely magmatic crystallization of the primary pegmatitic assemblage. The residual melt enriched in H_2O and network modifying elements starts to unmix an aqueous melt. **b:** In stage II, two liquids coexist. The aqueous melt alters parts of the primary assemblage to a phyllic quartz-muscovite assemblage (QM-A). Breakdown of primary minerals reincorporates rare elements into the residual melts. **c:** A hydrothermal fluid is released at some point. It causes further alteration and resorption of primary minerals. Local shift to hydrostatic pressure causes hydraulic fracturing. The temperature difference between core and margin facilitates fluid transport by convection. **d:** During stage III, albitite is precipitated from hydrothermal fluid. The fluid transports remobilized elements and causes greisenization and tourmalinization of the host rocks. Element transfer from the host rock might be possible, but was not assessed in this study. Cross sectional view. Based on the spodumene pegmatite solidification model for SE Ireland by Barros (2017).

1546

1547

1548

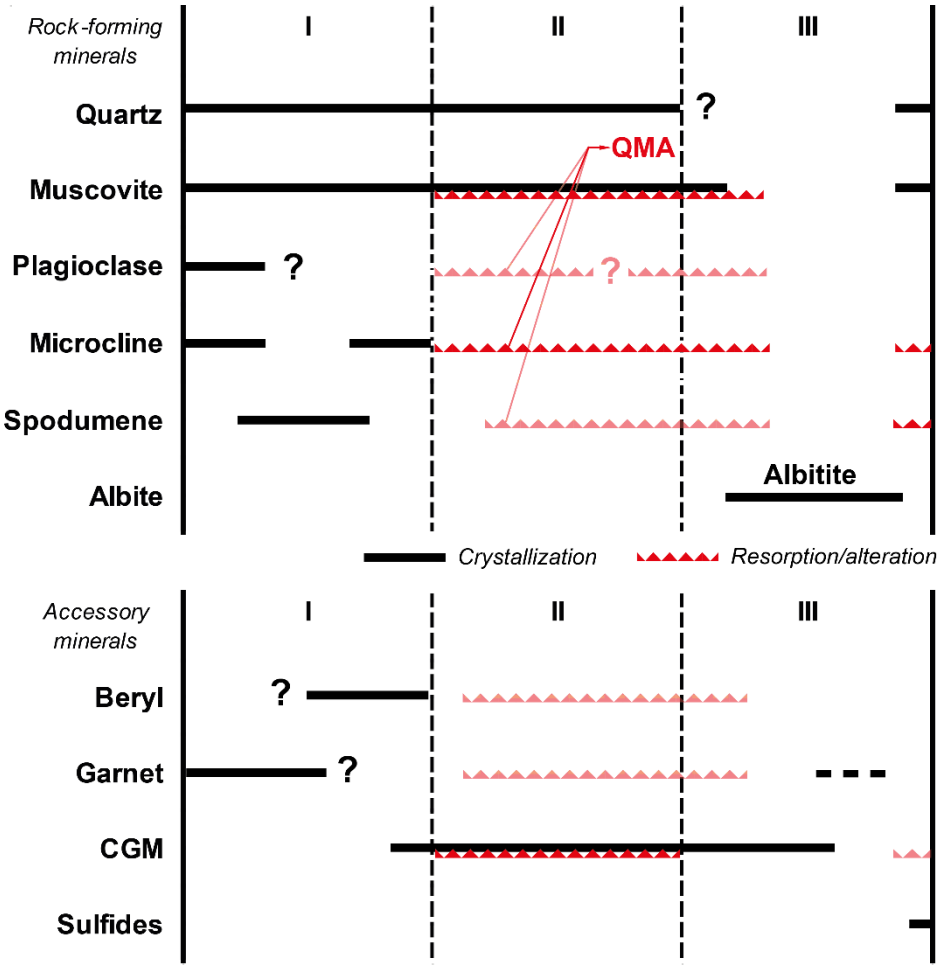

Fig. 17: Paragenetic sequence for rock-forming and accessory mineral crystallization and resorption/alteration during the three stages (I–III) of rare-element pegmatite formation. QMA: Onset of phyllic alteration and crystallization of quartz-muscovite assemblage.

1549

Table 1: Summary of all analyzed samples and minerals.

Sample	Lith.	Mineral	Comment
UB-A	b	*Muscovite*	
		Ms-1	Associated with several muscovite flakes in albitite.
		Ms-2	In paragenesis with CGM.
		Ms-3	CGM inclusion.
QM-A	c	*Muscovite*	
		Ms-1	In contact to multiple coarse muscovite flakes.
		Ms-2	Ms-2a in contact with beryl, replaced by Ms-2b.
		Ms-3	Located between albitite and quartz–muscovite assemblage.
LB-A	b	*Muscovite*	
		Ms-1	In contact with microcline, albite and CGM.
		Ms-2	In albite matrix; CGM inclusions.
		Ms-3	Fine-grained; filling feldspar fractures.
		Albite	
		Ab-1–3	Albitite-forming elongate-prismatic grains.
		Microcline	
		Kfs-1–3	Remnant perthitic microcline with diffuse crosshatch twinning.
		CGM	
		CGM-1	Oscillatory zoning; truncation.
		CGM-2	Oscillatory and complex zoning; truncation.
		CGM-3	Complex zoning; truncation.

Lithologies: b) albitite; c) quartz-muscovite assemblage.
CGM: columbite group mineral (columbite–tantalite).

Table 2: Major and minor element composition of muscovite in samples UB-A, QM-A and LB-A as determined by SEM-EDS. Concentrations are presented in wt.%. Cation calculation on basis of 20 oxygen atoms (excl. OH) using the following assumptions: $Al^{IV} = 8$ - Si; $Al^{VI} = Al_{total} - Al^{IV}$; $OH^{*} = 4$ - F; $Li2O^{*} = 0.3935\ F^{1.236}$ (Tischendorf et. al 1997).

	Upper-border albitite (UB-A)						Quartz–muscovite assemblage (QM-A)								Lower-border albitite (LB-A)					
	Ms-1	1σ	Ms-2	1σ	Ms-3	1σ	Ms-1	1σ	Ms-2a	1σ	Ms2-b	1σ	Ms-3	1σ	Ms-1	1σ	Ms-2	1σ	Ms-3	1σ
		n=5		n=4		n=6		n=9		n=6		n=3		n=3		n=4		n=3		n=3
SiO_2	45.51	0.09	45.25	0.23	45.59	0.39	45.45	0.13	45.45	0.08	48.22	2.06	45.52	0.18	45.49	0.10	45.39	0.10	47.55	0.96
Al_2O_3	35.79	0.14	35.75	0.43	35.32	0.68	33.53	0.21	33.38	0.33	21.49	0.89	34.02	0.12	35.20	0.29	35.44	0.05	36.34	0.84
FeO	1.48	0.07	1.37	0.24	1.67	0.36	3.44	0.19	3.41	0.17	8.81	1.39	3.03	0.08	2.08	0.15	1.96	0.03	0.31	0.16
MnO	0.13	0.01	0.14	0.04	0.18	0.04	0.36	0.03	0.37	0.02	1.12	0.16	0.32	0.02	0.11	0.03	0.11	0.02	0.03	0.02
MgO	0.09	0.02	0.09	0.03	0.10		0.03	0.01	0.03	0.01	0.16	0.12	b.d.		0.11	0.01	b.d.		b.d.	
CaO	0.07	0.02	0.08	0.01	0.08	0.02	0.07	0.01	0.08	0.02	0.07	0.02	0.06	0.00	0.09	0.01	0.07	0.01	0.07	0.02
Na_2O	0.48	0.06	0.43	0.05	0.45	0.04	0.42	0.05	0.40	0.02	0.14	0.04	0.48	0.06	0.44	0.04	0.42	0.03	0.44	0.06
K_2O	10.55	0.18	10.65	0.12	10.63	0.09	10.63	0.11	10.63	0.06	10.44	0.16	10.69	0.07	10.80	0.05	10.79	0.03	10.57	0.27
Rb_2O	0.58	0.25	0.74	0.12	0.49	0.16	0.60	0.10	0.42	0.16	0.53	0.16	0.32	0.08	0.51	0.12	0.36	0.06	0.29	0.13
Cs_2O	0.09	0.08	0.10	0.07	0.03	0.03	0.05	0.02	0.06	0.04	0.19	0.05	0.03	0.03	0.03	0.03	0.04	0.02	b.d.	
F	0.49	0.08	0.52	0.06	0.56	0.05	1.00	0.09	1.01	0.06	4.37	0.83	0.85	0.03	0.45	0.05	0.39	0.03	b.d.	
Sum	95.26		95.12		95.10		95.60		95.21		95.53		95.32		95.30		94.98		95.60	
Li_2O^{*}	0.15	0.03	0.17	0.03	0.18	0.02	0.39	0.05	0.40	0.03	2.78	0.70	0.32	0.01	0.14	0.02	0.11	0.01		
H_2O^{*}	4.23	2.94	4.19	2.07	4.18	1.60	3.93	1.62	3.92	1.07	2.17	3.44	4.01	0.63	4.22	1.99	4.25	1.39	4.54	
O=F	0.21		0.22		0.24		0.42		0.43		1.84		0.36		0.19		0.16			
Sum^{*}	99.43		99.26		99.22		99.50		99.10		98.64		99.30		99.47		99.18		100.14	
Si	6.121		6.107		6.147		6.184		6.198		6.815		6.179		6.137		6.130		6.206	
Al_{IV}	1.879		1.893		1.853		1.816		1.802		1.185		1.821		1.863		1.870		1.794	
$\sum_T$	8.000		8.000		8.000		8.000		8.000		8.000		8.000		8.000		8.000		8.000	
Al_{VI}	3.796		3.795		3.761		3.562		3.564		2.395		3.621		3.735		3.772		3.925	
Fe	0.166		0.155		0.188		0.392		0.389		1.041		0.344		0.235		0.222		0.030	
Mn	0.015		0.015		0.021		0.042		0.043		0.134		0.036		0.013		0.013		0.003	
Mg	0.018		0.019		0.020		0.007		0.006		0.033				0.022					
Li^{*}	0.082		0.090		0.099		0.216		0.219		1.582		0.174		0.075		0.061			
$\sum_Y$	**4.077**		**4.074**		**4.089**		**4.219**		**4.221**		**5.185**		**4.175**		**4.079**		**4.068**		**3.957**	
Ca	0.010		0.012		0.011		0.011		0.011		0.011		0.009		0.012		0.010		0.010	
Na	0.124		0.113		0.118		0.111		0.106		0.037		0.126		0.116		0.111		0.113	
K	1.810		1.833		1.828		1.845		1.848		1.882		1.851		1.858		1.858		1.798	
Rb	0.050		0.064		0.042		0.052		0.036		0.048		0.028		0.044		0.031		0.023	
Cs	0.005		0.006		0.002		0.003		0.003		0.011		0.002		0.001		0.002			
$\sum_X$	**1.999**		**2.028**		**2.001**		**2.022**		**2.004**		**1.989**		**2.016**		**2.031**		**2.012**		**1.944**	
OH^{*}	3.792		3.777		3.760		3.569		3.564		2.045		3.634		3.807		3.833		4.000	
F	0.208		0.223		0.240		0.431		0.436		1.955		0.366		0.193		0.167		0.000	
$\sum_A$	4.000		4.000		4.000		4.000		4.000		4.000		4.000		4.000		4.000		4.000	
$\sum_{X+Y+T+A}$	**18.076**		**18.102**		**18.090**		**18.241**		**18.225**		**19.174**		**18.191**		**18.111**		**18.081**		**17.901**	

b.d.: below detection limit

*calculated, 1σ propagated from 1σ for F

Table 3: Albite (Ab1–3) and microcline (Kfs1–3) composition in sample LB-A as determined by SEM-EDS. Element oxide concentrations in wt%; endmember concentrations in mol.%. Cation calculations on basis of 8 oxygen atoms.

	Albite						Microcline					
	LB-A	1σ	LB-A	1σ	LB-A	1σ	LB-A	1σ	LB-A	1σ	LB-A	1σ
	Ab-1	n=3	Ab-2	n=4	Ab-3	n=3	Kfs-1	n=5	Kfs-2	n=4	Kfs-3	n=6
SiO_2	67.70	0.53	68.21	0.35	68.23	0.21	63.84	0.21	64.18	0.21	64.00	0.16
Al_2O_3	19.91	0.27	19.82	0.05	19.94	0.08	18.84	0.11	19.10	0.06	19.00	0.07
P_2O_5	b.d.		b.d.		b.d.		0.27	0.14	0.37	0.04	0.34	0.05
CaO	0.08	0.08	b.d.		0.04	0.04	0.08	0.02	0.08	0.02	0.06	0.05
Na_2O	11.27	0.09	11.29	0.11	11.39	0.09	0.62	0.06	0.95	0.10	0.86	0.15
K_2O	0.08	0.02	0.15	0.04	0.12	0.07	16.19	0.13	15.58	0.18	15.90	0.33
Sum	99.03		99.46		99.72		99.84		100.26		100.16	
Si	2.982		2.989		2.985		2.964		2.960		2.960	
Al	1.033		1.024		1.028		1.031		1.038		1.036	
P							0.005		0.007		0.007	
$\sum_T$	**4.015**		**4.013**		**4.013**		**4.001**		**4.005**		**4.002**	
Ca	0.004				0.002		0.004		0.004		0.003	
Na	0.962		0.959		0.966		0.056		0.085		0.077	
Ka	0.004		0.008		0.007		0.959		0.917		0.938	
$\sum_X$	0.970		0.970		0.974		1.019		1.005		1.018	
$\sum_{T+X}$	**4.985**		**4.983**		**4.987**		**5.019**		**5.010**		**5.020**	
An	0.37		0.00		0.19		0.39		0.38		0.29	
Ab	99.17		99.16		99.12		5.50		8.41		7.60	
Or	0.46		0.84		0.69		94.11		91.21		92.11	

n: measurements per grain.
b.d.: below detection limit.

1553

Table 4: Composition of columbite group minerals (CGM) in sample LB-A as determined by SEM-EDS. Element oxide concentrations in wt%. Cation calculations on basis of 6 oxygen atoms for the stoichiometric formula XY_2O_6.

	LB-A-CGM-1			LB-A-CGM-2			LB-A-CGM-3		
	1	2	3	1	2	3	1	2	3
Ta_2O_5	21.17	20.18	40.60	22.36	19.12	36.99	28.45	28.18	47.79
Nb_2O_5	58.87	60.21	40.40	58.65	60.90	43.09	51.20	53.17	31.20
FeO	7.23	9.08	8.32	8.27	8.09	8.53	10.02	9.38	9.62
MnO	12.10	10.34	9.57	11.04	11.30	9.54	8.75	9.08	8.25
Sum	99.37	99.82	98.89	100.32	99.41	98.14	98.43	99.81	96.87
Ta	0.36	0.34	0.75	0.37	0.32	0.68	0.50	0.49	0.94
Nb	1.64	1.66	1.24	1.63	1.68	1.31	1.49	1.52	1.02
$\sum_Y$	**2.00**	**2.00**	**1.99**	**2.00**	**2.00**	**1.99**	**1.99**	**2.01**	**1.96**
Fe	0.37	0.46	0.47	0.42	0.41	0.48	0.54	0.50	0.58
Mn	0.63	0.54	0.55	0.57	0.58	0.54	0.48	0.49	0.51
$\sum_X$	**1.01**	**1.00**	**1.02**	**1.00**	**1.00**	**1.03**	**1.02**	**0.98**	**1.09**
$\sum_{X+Y}$	**3.00**	**3.00**	**3.01**	**3.00**	**3.00**	**3.02**	**3.01**	**2.99**	**3.05**
Ta#	0.18	0.17	0.38	0.19	0.16	0.34	0.25	0.24	0.48
Mn#	0.63	0.54	0.54	0.57	0.59	0.53	0.47	0.50	0.46

Ta# = Ta/(Ta+Nb)
Mn# = Mn/(Mn+Fe)

1554

1555

1556

Table 5: Mineral/melt and fluid melt/partition coefficients k_d for K, Rb, Cs, Nb and Ta including references (a–h). Partition coefficients are for the respective mineral/fluid in peraluminous granitic, rhyolitic, or pegmatitic melt, unless stated otherwise.

Element	Muscovite		Alkali feldspar		Albite		Quartz		Fluid	
K	2.52	a	3.13	b	0.10	d*	0.013	f	0.10	g
Rb	1.61	a	1.30	c	0.04	e	0.014	f	0.45	f
Cs	0.21	a	0.16	b	0.04	e	0.029	f	0.50	f
Nb	3.50	g			0.10	h'	0.010	‡	0.08	i
Ta	0.42	g			0.13	h'	0.010	‡	0.08	‡
References	a: Icenhower & London (1996); b: Icenhower & London (1995); c: Walker et al. 1989; d: Philpotts & Schnetzler (1970); e: Joliff et al. (1992); f: Nash & Crecraft (1985); g: London(2005); g: Raimbault & Burnol 1998; h: Bea et al. (1994); i: Linnen & Cuney (2005).									

*Plagioclase in andesite.
'Plagioclase in peraluminous migmatite.
‡Assumed.

1557

Table 6: Results from geochemical modelling for the trace element distribution in profile B–A for each zone of muscovite LB-A-Ms-2. **a:** Slope (m) and (b) from linear regression of the data, as well as modeled values for *m*, *b* and residual melt at the end of each zone F_{end}. **b:** bulk partition coefficients for best solutions for modeled *m* and *b* or best fit of the observed concentration trend (parentheses) **c**: Initial melt/fluid composition. **d:** melt/fluid composition at F_{end}. Bulk partition coefficients and concentrations in brackets fit the actual observed profile best, while they yield poor solutions for *m* and *b*.

a	From regression		Model		F_{end}
Zone	*m*	*b*	*m*	*b*	
I.3	-0.361	2.30	-0.361	2.30	0.42
II.1	-0.652	3.09	0.652 (-0.068)	3.09 (1.36)	0.93
II.2	-0.612	2.98	0.612 (-0.303)	2.98 (2.06)	0.82
II.3	-0.566	2.84	-0.566 (-0.327)	2.83 (2.10)	0.77
III.1	-0.165	1.82	-0.165 (-0.280)	1.73 (2.06)	0.63
III.2	-0.048	1.57	-0.045	1.39	0.85

b	Bulk partition coefficients				
Zone	D_K	D_{Rb}	D_{Cs}	D_{Nb}	D_{Ta}
I.3	1.004	0.710	0.173	0.90	1.10
II.1	1.68 (1.05)	1.205 (1.001)	0.279	1.80	0.10
II.2	1.48 (0.70)	0.93 (0.43)	0.109	0.10	0.01
II.3	1.38 (1.16)	0.870	0.103	2.00	0.001
III.1	0.76 (0.85)	0.640	0.250	0.20	0.28
III.2	0.90	1.120	5.250	1.30	3.20

c	Initial melt/fluid composition (F = 1)				
Zone	K [wt%]	Rb [ppm]	Cs [ppm]	Nb [ppm]	Ta [ppm]
I.3	3.57	3100	4800	39	224
II.1	3.52	3900	5635	50	85
II.2	3.50	3830	5550	47	158
II.3	3.68	4430	6720	52	115
III.1	3.50	2100	1980	52	170
III.2	3.51	1960	2850	29	180

d	Melt/fluid composition at F_{end}				
Zone	K [wt%]	Rb [ppm]	Cs [ppm]	Nb [ppm]	Ta [ppm]
I.3	3.56	4002	9835	43	205
II.1	3.35 (3.50)	3840 (3900)	5940	47	91
II.2	3.18 (3.71)	3880 (4290)	6620	56	192
II.3	3.34 (3.53)	4590	8495	40	149
III.1	3.90 (3.75)	2480	2800	36	237
III.2	3.55	1920	430	28	126

1558